

# Self-mixing in microtubule-kinesin active fluid from nonuniform to uniform distributions of activities

Teagan E Bate,<sup>1</sup> Megan E Varney,<sup>2</sup> Ezra H Taylor,<sup>1</sup> Joshua H Dickie,<sup>1</sup> Chih-Che Chueh,<sup>3</sup> Michael M Norton,<sup>4</sup> and Kun-Ta Wu<sup>1,5,6,\*</sup>

<sup>1</sup>Department of Physics, Worcester Polytechnic Institute, Worcester, Massachusetts 01609, USA

<sup>2</sup>Department of Physics, New York University, New York, New York 10003, USA

<sup>3</sup>Department of Aeronautics and Astronautics, National Cheng Kung University, Tainan 701, Taiwan

<sup>4</sup>School of Physics and Astronomy, Rochester Institute of Technology, Rochester, New York 14623, USA

<sup>5</sup>Department of Mechanical Engineering, Worcester Polytechnic Institute, Worcester, Massachusetts 01609, USA

<sup>6</sup>The Martin Fisher School of Physics, Brandeis University, Waltham, Massachusetts 02454, USA

\*Corresponding: [kwu@wpi.edu](mailto:kwu@wpi.edu)

## Abstract

Active fluids have potential applications in micromixing, but little is known about the mixing kinematics of systems with spatiotemporally varying activities. Ultraviolet light-activated caged ATP and fluorescent dyes were used to activate controlled regions of microtubule-kinesin active fluid, creating a binary active-inactive fluid where the progression of mixing was observed. At low flow-speed levels, mixing was governed by active fluid-induced diffusion-like processes at the active-inactive interface, but at higher flow-speed levels, mixing was governed by active fluid-induced superdiffusion-like processes. Samples activated in a checkerboard pattern reached homogeneity faster than those that were activated only on one side. A model of active nematic hydrodynamics coupled to ATP transport was used to describe the coupled mixing process. The results show that the mixing of active fluid systems with initially nonuniform activities is governed by the complex active transport of ATP at the interface between active and inactive regions.

## Introduction

Miniaturization enhances production efficiency in chemical engineering, biological engineering, and pharmaceutical manufacturing.<sup>1</sup> For example, microreactors—millimeter-scale devices that use channels to mix chemicals and induce chemical reactions—are used to synthesize materials,<sup>2</sup> test enzymes,<sup>3</sup> and analyze protein conformations.<sup>4</sup> These devices require mixing to homogenize reactants, but it is challenging to achieve mixing at the micron scale (micromixing) because fluid dynamics at that scale are dominated by laminar flow.<sup>5</sup> At the macroscopic scale, turbulence-induced advection plays the dominant role in mixing by repeatedly stretching and folding the components until a uniform state is reached<sup>6</sup>; however, at the microscopic scale where the Reynolds number is low ( $\ll 1$ ), turbulence is inhibited<sup>5</sup> and mixing is dominated by molecular diffusion, which is slow and difficult to control. Approaches such as serpentine design,<sup>7</sup> vibrating bubbles,<sup>8</sup> and viscoelastic polymers<sup>9</sup> have been developed to enhance mixing at a microscopic scale, but these approaches are driven by external energy sources and thus require external components that limit miniaturization.<sup>1,10,11</sup>

A potential strategy to achieve mixing at the micron scale is to apply active fluids: fluids whose constituents consume local fuel to generate movement.<sup>12-20</sup> The flows of these active fluids self-organize into active turbulence<sup>21-23</sup> that promotes micromixing by repeatedly stretching and folding fluid even in low Reynolds number systems.<sup>24</sup> A number of studies have characterized active fluid-induced mixing in microtubule-based active nematics and computationally explored the process for dilute suspensions of swimmers<sup>24-26</sup>; however, these studies focused on systems with uniform activity. Mixing is a process of transition from a nonuniform to uniform state; therefore, mixing tasks generally start from a nonuniform state. Active systems with nonuniform but stationary activity exhibit dynamics distinct from those with uniform activity.<sup>27-33</sup> These dynamics become particularly rich when activity varies in space and time<sup>31,32</sup> and the

evolution of the activity field couples to the active flow.<sup>27-29</sup> However, such mixing dynamics with complex coupling between activity field and active flow remains poorly understood. To study fluid and mixing dynamics in a system with nonuniform activity and spatiotemporally coupled activity distribution and fluid flow, we investigated how activated active fluid mixed and blended with inactivated active fluid until the system reached a uniform state and employed active nematohydrodynamic and mass-transport models to describe the mixing process.

## Results

**Active and inactive fluids self-mix into a homogeneous active fluid.** We used microtubule-kinesin active fluid for these investigations because it enhances micromixing,<sup>15,24</sup> has tunable and robust activity,<sup>34-39</sup> and has many established models describing its flow behaviors.<sup>40-42</sup> In microtubule-kinesin active fluid, self-extending microtubule bundles drive chaotic vortical flows. Extension is driven locally by kinesin motor dimers that hydrolyze ATP to “walk” along pairs of antiparallel microtubules and force them in opposite directions (Fig. 1a).<sup>15</sup> To create a system with an activated active fluid adjacent to an inactivated active fluid, we synthesized microtubule-kinesin active fluid<sup>15,43</sup> but replaced the ATP with caged ATP whose terminal phosphate was esterified with a blocking group (Fig. 1b). This caged ATP could not be hydrolyzed by kinesin motors until the blocking group was removed by exposure to ultraviolet (UV) light.<sup>44,45</sup> The initially inactivated fluid was loaded into a rectangular flow cell ( $20 \times 4 \times 0.1 \text{ mm}^3$ ). To activate the fluid and create an active-inactive interface, we applied UV light to one side of the sample, which released the ATP and activated the fluid on that side of the sample (Fig. 1c; Supplementary Video 1). The activated region then gradually expanded and invaded the inactivated region until the activity in the system was uniformly distributed (Fig. 1c). To quantify the evolution of the activity distribution, we doped the fluid with fluorescent tracers and monitored the tracer motion to extract the speed distribution of active fluid flows (Fig. 1d). The speed distribution showed that the active fluid was initially quiescent (speed = 0, Fig. 1d top panel); after UV exposure, the UV-exposed active fluid was active (second panel); then the active area expanded toward the inactive area (third panel) until the speed was uniformly distributed (bottom panel). The normalized speed profile (Fig. 1e) was initially like a step function (red curve), indicating a sharp interface between active and inactive fluids, and then the interface widened and shifted as active fluid blended with inactive fluid (black curve).

**Is the mixing dynamics of active and inactive fluids governed by superdiffusion-like process?** Active turbulence can enhance the motions of tracers from being diffusion-like (where tracer’s mean squared displacement [MSD] is proportional to time lapse:  $\text{MSD} \sim \Delta t^\alpha$  with  $\alpha = 1$ ) to superdiffusion-like ( $\alpha > 1$ ),<sup>15,26,34</sup> which suggests that active fluid flows can promote micromixing performance. Thus, we hypothesized that the mixing dynamics of active and inactive fluids is governed by a superdiffusion-like process of ATP driven by active fluid at the active-inactive interface. To test this hypothesis, we analyzed the displacement of the active-inactive fluid interface as a function of time (Fig. 2a inset), which showed that the shifting of the interface decelerated as the active fluid mixed with the inactive fluid. To determine whether the mixing process is governed by superdiffusion-like processes, we analyzed the squared interface displacement ( $\Delta x^2$ ) as a function of time (Fig. 2a), which showed that at the long timescale ( $\Delta t \gtrsim 200 \text{ s}$ ), the squared interface displacement was approximately proportional to time:  $\Delta x^2 \sim \Delta t^\gamma$  with interface progression exponent  $\gamma \approx 1$  (Fig. 2a). To demonstrate that this result was independent of caged ATP concentration, we repeated the  $\gamma$  measurement while varying caged ATP concentrations from 0.5 to 8 mM and found that the result of  $\gamma \approx 1$  remained invariant across this range (Fig. 2b). Notably, while the diffusive

time-scaling  $\gamma$  remained consistent, the prefactor  $P_I$  exhibited a monotonic dependence on caged ATP concentration (Fig. 2c).

**At low flow-speed levels, the mixing process of active and inactive fluids is governed by diffusion-like processes of ATP at the active-inactive interface.** Next, we examined whether the result of  $\gamma \approx 1$  was the consequence of superdiffusion-like processes ( $\text{MSD} \sim \Delta t^a$  with  $a > 1$ ) of ATP at the active-inactive interfaces. It would have been ideal to use an active fluid model that describes the complex mixing process at the active-inactive interface whose position and width change with time; however, such a model was not yet available. Thus, to test our hypothesis, we developed a simple model that assumes that the ATP dispersion is governed only by a diffusion-like process ( $a = 1$ ), a process slower than superdiffusion. If the model predicted a smaller  $\gamma$  than experimental observation, ( $\gamma < 1$ ), that would suggest that the mixing process was governed by a process faster than diffusion (i.e. superdiffusion), and thus support the hypothesis. Herein, we modeled the ATP dispersion process with Fick's law of diffusion:

$$\frac{\partial C(\mathbf{r}, t)}{\partial t} = D \nabla^2 C(\mathbf{r}, t), \quad 1$$

where  $C(\mathbf{r}, t)$  represents the spatial distribution of ATP concentrations at time  $t$  and  $D$  is the effective diffusion coefficient of ATP in active fluid. We chose  $D = 7 \times 10^{-10} \text{ m}^2/\text{s}$ , the ATP diffusion coefficient in water,<sup>46</sup> because our active fluid is 96% water<sup>47</sup> and thus has a viscosity similar to that of water.<sup>48</sup> To simplify the modeling, we considered a one-dimensional active fluid system confined in a segment,  $x = 0 - L$ , where  $L$  is the segment length, which was  $L = 20 \text{ mm}$  in our experiments (Figs. 1c & d). The confinement indicated no-flux boundary conditions:

$$\frac{\partial}{\partial x} C(x = 0, t) = \frac{\partial}{\partial x} C(x = L, t) = 0. \quad 2$$

To mimic the UV-activation process in the experiment (Fig. 1c), we initiated the ATP concentration with a step function:

$$C(x, t = 0) = \frac{C_0}{2} \text{erfc} \left( \frac{x - x_0}{2\sqrt{\epsilon D}} \right), \quad 3$$

where  $C_0 = 0.5\text{--}8 \text{ mM}$ , the initial ATP concentrations in the UV-activated region; erfc is the complementary error function; and  $x_0 = 10 \text{ mm}$  is the initial position of the active-inactive interface. We chose  $\epsilon = 0.001$  to generate a sharp concentration transition at the interface. Then we numerically solved Fick's diffusion equation (Eq. 1) with these initial and boundary conditions (Eqs. 2 and 3) to determine the spatial and temporal distribution of ATP concentrations (Fig. 3a; Supplementary Video 2) which showed that the ATP was initially distributed only on one side of the system (red) and then dispersed to the inactive region (black) until it was uniformly distributed.

ATP concentrations can control the flow-speed level of active fluid<sup>15,34</sup>; thus, we modeled the ATP-dependent flow-speed level with Michaelis-Menten kinetics:

$$\bar{v} = \bar{v}_m \left( \frac{[\text{ATP}]}{[\text{ATP}] + K} \right), \quad 4$$

where  $\bar{v}$  is the mean speed of active fluid;  $\bar{v}_m = 6.2 \text{ }\mu\text{m/s}$ , the saturated mean speed; and  $K = 270 \text{ }\mu\text{M}$ , the ATP concentration that leads to half of the saturated mean speed,  $\bar{v}_m/2$ .<sup>49</sup> The fluid-gel transition of the

microtubule network was neglected to simplify the model, which may lead the model to overestimate the fluid speed at low ATP concentrations (see Discussion).<sup>48,50</sup> Using this ATP-activity equation (Eq. 4), we converted the ATP distribution to the mean speed distribution of active fluid (Fig. 3b; Supplementary Video 2), which showed that initially one side of the fluid sample was activated (red) and then the fluid evolved toward a uniformly activated state (black). The mean speed distribution shows the advancement of the active-inactive interface (Fig. 3c inset) and the squared interface displacement that increased linearly with time,  $\Delta x^2 \sim \Delta t$  (Fig. 3c), which is consistent with our experimental observation of  $\gamma \approx 1$  (Figs. 2a & 2b). This diffusion-based model was consistent with our experimental data, which suggests that the mixing dynamics at the active-inactive fluid interface was governed by a diffusion-like process of ATP rather than superdiffusion. This invalidated our hypothesis that the mixing dynamics of active and inactive fluids is governed by superdiffusion-like processes of ATP.

To further confirm the diffusion-like process in the ATP dispersion, we analyzed the interface progression coefficients  $P_I$  for both our experiments and models by fitting the  $\Delta x^2$  versus  $\Delta t$  data to  $\Delta x^2 = 2P_I\Delta t$  with  $P_I$  as the fitting parameter (Figs. 2c & 3c) and normalized the coefficients by their values at 8 mM ATP,  $P_{I0}$  (Fig. 3d). This showed that the interface progression coefficients in both the experiments (blue dots) and models (red dots) increased with ATP concentration and were scaled consistently. This consistent scaling reinforced the assertion that the ATP dispersion at this flow-speed level was governed by a diffusion-like process. This consistency between the model predictions and the experimental results showed that a model based on Fick's law and the nonlinear relationship between ATP and flow speed was sufficient to capture the mixing process between active and inactive fluids at this flow-speed level, without the need to introduce complex active nematohydrodynamic equations.<sup>41</sup>

**Superdiffusion-like processes in mixing at active–inactive interfaces only emerge when the flow-speed level of the active fluid is sufficiently high.** At this point, our data and model suggested that the mixing process of active and inactive fluids was governed by a diffusion-like process; this was contrary to our expectation, because existing studies showed that active fluid exhibited superdiffusive-like behaviors in mixing components.<sup>15,26,34</sup> However, the previous studies investigated systems with uniform activity, whereas our system had nonuniform activity. With this in mind, we developed a second hypothesis: the mixing of active and inactive fluids is governed by an active fluid-induced superdiffusion-like process only when the flow-speed level of the active fluid is sufficiently high.<sup>27,28</sup> To test this hypothesis, we performed the same experiments while varying the flow-speed level of the active fluid in the initial UV-activated region, quantified as the average of flow speeds in the bulk of the initially activated area,  $\bar{v}_{ab}$ . Because the interface progression could be affected by ATP concentrations (Fig. 3d), we kept the caged ATP concentration constant (5 mM) while varying  $\bar{v}_{ab}$ . To decelerate the active fluid, we replaced fractions of the processive motors (K401) with nonprocessive motors (K365). Processive motors exert a force on microtubules continuously, whereas nonprocessive motors detach after each force application and thus drive the microtubules more slowly (Fig. 4 inset left).<sup>35,49</sup> To accelerate the active fluid, we increased the sample thickness, because a thicker sample container decreases hydrodynamic drag and allows the active fluid to flow faster (Fig. 4 inset right).<sup>49,51</sup> Then we analyzed the active-inactive interface progression exponent  $\gamma$  as a function of  $\bar{v}_{ab}$  (Fig. 4), which showed that the exponent remained at  $\gamma \approx 1$  at low flow-speed levels ( $\bar{v}_{ab} \lesssim 5 \text{ } \mu\text{m/s}$ ) and increased monotonically to  $\gamma \approx 1.7$  as the flow-speed level increased ( $\bar{v}_{ab} \gtrsim 5 \text{ } \mu\text{m/s}$ ). The results of  $\gamma > 1$  as  $\bar{v}_{ab} \gtrsim 5 \text{ } \mu\text{m/s}$  suggested that as the active fluid flowed sufficiently fast ( $\gtrsim 5 \text{ } \mu\text{m/s}$ ), a superdiffusion-like process started to emerge and govern the mixing between active and inactive fluids at their interfaces, which agreed with our second hypothesis.

**Elevating flow-speed levels of active fluid reduces the mixing time of UV-activated fluorescent dyes.** To further confirm our second hypothesis, that mixing is governed by active fluid-induced superdiffusion-like processes only at high flow-speed levels, we designed another series of experiments to characterize how well the active-inactive fluid system could mix suspended components that were initially nonuniform. We chose UV-activated fluorescent dyes as our suspended components because their initial state could be controlled with the same light source as the caged ATP. We exposed one side of the sample to UV light to activate both the active fluid and fluorescent dye on that side of the sample and monitored the distribution of activated fluorescent dyes as they dispersed. We found that in an inactive fluid sample ( $\bar{v}_{ab} = 0$ ) where dyes dispersed only by molecular diffusion, the dyes barely dispersed, whereas in an active fluid where one side of the sample was activated ( $\bar{v}_{ab} = 8.2 \mu\text{m/s}$ ), the dyes were transported by active fluid flows (active transport) and dispersed through the sample in 4 hours (Fig. 5a). To quantify the dispersion rate, we adopted Saintillan and Shelley's method to analyze the normalized multiscale norm of dye brightness as a function of time<sup>25</sup>:  $\hat{s}(t) \equiv |s(t)|/|s(0)|$ , where

$$|s| \equiv \left[ \sum_k \frac{|s_k|^2}{\sqrt{1 + l^2 k^2}} \right]^{1/2}, \quad 5$$

$s_k$  is the Fourier coefficient at wave vector  $\mathbf{k}$  in a Fourier expansion of the dye brightness and  $l = 4.84 \mu\text{m}$ , the pixel size of the micrographs. We analyzed the evolution of the normalized multiscale norm for various samples with  $\bar{v}_{ab} = 0\text{--}8.2 \mu\text{m/s}$ , which revealed that the normalized multiscale norm decayed faster as  $\bar{v}_{ab}$  increased (Fig. 5b). The norm was reported to decay exponentially,<sup>25</sup> so we quantified the decay rate by fitting the first hour  $\hat{s}(t)$  data to  $\ln \hat{s} = -t/t_0$  with  $t_0$  (mixing time) as the fitting parameter (Fig. 5b inset).

We found that at low flow-speed levels ( $\bar{v}_{ab} \lesssim 6 \mu\text{m/s}$ ), the mixing time decreased slowly with increasing  $\bar{v}_{ab}$  (from 7.5 to 6 h); but after the flow speed passed a threshold ( $\bar{v}_{ab} = 6 \mu\text{m/s}$ ), the mixing time dropped rapidly (to 2 h) (Fig. 5c). The interface progression exponent showed a similar transition ( $\bar{v}_{ab} \approx 5 \mu\text{m/s}$ ; Fig. 4). These results showed a transition in mixing mechanisms from diffusion-like to superdiffusion-like processes and thus supported our hypothesis that a minimum flow-speed level is required for superdiffusion-like mechanisms to emerge.

**At low flow-speed levels, mixing at active–inactive interfaces was governed by active fluid-induced diffusion-like processes rather than molecular diffusion.** Both the dye experiments and interface progression experiments showed a transition in mixing mechanism from diffusion-like to superdiffusion-like processes (Figs. 4 & 5c), but whether the diffusion-like process in this context represented molecular diffusion or an active fluid-induced diffusion-like process remained unclear. Both processes have MSD of ATP molecules proportional to time ( $\text{MSD} \sim t$ ), but molecular diffusion is driven by thermal fluctuation whereas an active fluid-induced diffusion-like process is governed by low flow-speed active fluid transporting ATP molecules in a chaotic way such that their MSD is proportional to time lapse with a higher effective diffusion coefficient.<sup>15,26,34</sup> To elucidate the underlying mechanisms of ATP dispersion at active–inactive interfaces, we compared the mixing time in an inactive fluid system ( $t_0 = 24 \text{ h at } \bar{v}_{ab} = 0$ ), where mixing was driven only by molecular diffusion, with that in the minimally activated fluid ( $t_0 = 7.5 \text{ h at } \bar{v}_{ab} = 2 \mu\text{m/s}$ ), where active transport additionally contributed to the mixing dynamics (Fig. 5c inset). We found that mixing time in mixing driven by molecular diffusion and active transport was one-third as long as that driven only by molecular diffusion (7.5 h vs. 24 h). These results suggest that molecular diffusion does not make a major contribution to mixing in active fluid systems; the mixing was mainly driven by

active transport at the active-inactive interface, which performs diffusion-like mixing at low flow-speed levels and superdiffusion-like mixing at high flow-speed levels.<sup>15,26,34</sup>

**Continuous active fluid model captures the mixing of nonuniform active fluid systems.** Our data suggested that mixing in an activity-nonuniform system was governed by either diffusion-like or superdiffusion-like processes of ATP (Fig. 5c). To determine whether such a complex mixing process could be modeled with an existing active fluid model, we adopted Varghese *et al.*'s active fluid model<sup>52</sup> because it successfully describes the coherent-chaotic flow transition in 3D microtubule-kinesin active fluid systems.<sup>51</sup> The model describes microtubules as self-elongating rods whose nematic order,  $\mathbf{Q}$ , spontaneously decays due to the rods' rotational molecular diffusion where the rods' orientation is affected by solvent flow. We implemented the active fluid model using the relaxation rate of nematic order as the time scale and the nematic coherence length as the length scale.<sup>52</sup> Then, the dimensionless kinetic equation for  $\mathbf{Q}$  could be written as

$$\begin{aligned} \partial_{t^*} \mathbf{Q} + \mathbf{u} \cdot \nabla_* \mathbf{Q} + \mathbf{Q} \cdot \Omega^* - \Omega^* \cdot \mathbf{Q} \\ = - \left[ A_1 \mathbf{Q} + A_2 \left( \mathbf{Q}^2 - \frac{1}{d} \text{Tr}(\mathbf{Q}^2) \mathbf{I} \right) + A_3 \text{Tr}(\mathbf{Q}^2) \mathbf{Q} \right] + \nabla_*^2 \mathbf{Q} \\ + \lambda \left[ \frac{2}{d} \mathbf{E}^* + \mathbf{Q} \cdot \mathbf{E}^* + \mathbf{E}^* \cdot \mathbf{Q} - \frac{2}{d} \text{Tr}(\mathbf{Q} \cdot \mathbf{E}^*) \mathbf{I} \right], \end{aligned} \quad 6$$

where  $t^*$  is the dimensionless time;  $\nabla_*$  is the dimensionless spatial gradient operator;  $\nabla_*^2$  is the dimensionless Laplacian operator;  $\Omega^* \equiv [(\nabla_* \mathbf{u})^T - \nabla_* \mathbf{u}] / 2$  is the dimensionless vorticity tensor;  $\mathbf{E}^* \equiv [(\nabla_* \mathbf{u})^T + \nabla_* \mathbf{u}] / 2$  is the dimensionless strain rate tensor;  $A_i$ 's are the stabilization coefficients for flow alignment<sup>52</sup>;  $\lambda = 1$  is the flow alignment coefficient;  $d$  is the system dimensionality; and  $\mathbf{u}$  is the dimensionless flow velocity of incompressible solvent ( $\nabla_* \cdot \mathbf{u} = 0$ ), which satisfies the Stokes equation:

$$\nabla_*^2 \mathbf{u} - \nabla_* p^* - \nabla_* \cdot \boldsymbol{\sigma}_a = 0, \quad 7$$

where  $p^*$  is the dimensionless pressure and  $\boldsymbol{\sigma}_a \equiv \alpha^* \mathbf{Q}$ , the dimensionless active stress exerted by self-elongating rods with a dimensionless activity coefficient  $\alpha^*$ .<sup>53</sup> Because the activity coefficient increased with ATP concentration,<sup>54</sup> we selected an  $\alpha$ -ATP relationship<sup>55</sup>:

$$\alpha^* = \alpha_0^* \nu^\beta, \quad 8$$

where  $\alpha_0^*$  is the dimensionless activity level;  $\beta = 1$ , a scaling factor that depends on system characteristics such as length and elasticity of microtubules; and

$$\nu \equiv \frac{C}{C + K_m}, \quad 9$$

where  $C$  is the ATP concentration and  $K_m \approx 270 \mu\text{M}$  for our motors according to our previous measurements.<sup>49</sup> We selected this relationship because it captured the dynamics of microtubule bundle extension and kinesin kinetics (Michaelis-Menten), which play critical roles in the activity of microtubule-kinesin active fluid systems.<sup>56,57</sup> Finally, given that ATP diffused as a result of thermal fluctuation as well as flowed with the active fluid, we modeled ATP dispersion with a convection-diffusion equation:

$$\frac{\partial C(\mathbf{r}, t)}{\partial t^*} = D^* \nabla_*^2 C(\mathbf{r}, t) - \mathbf{u} \cdot \nabla_* C, \quad 10$$

where  $D^*$  is the dimensionless ATP molecular diffusion coefficient. To simplify modeling, we considered a 2D active fluid system ( $d = 2$ ;  $A_1 = 0.2$ ;  $A_2 = A_3 = 0$ )<sup>52</sup> confined in a  $250 \times 50$  rectangular boundary with no-slip boundary condition for flows ( $\mathbf{u} = \mathbf{0}$ ) and no-flux boundary condition for rods ( $\mathbf{n} \cdot \nabla_* \mathbf{Q} = \mathbf{0}$ , where  $\mathbf{n}$  represents a unit vector normal to boundaries). To solve the equations for  $\mathbf{Q}$ ,  $\mathbf{u}$ , and  $C$  (Eq. 6, 7, & 10), we determined the initial conditions as quiescent solvent ( $\mathbf{u} = \mathbf{0}$ ) under uniform pressure ( $p^* = 0$ ) with the rods in an isotropic state [ $Q_{xx} = -Q_{yy} = 5 \times 10^{-4} rn(\mathbf{r})$  and  $Q_{xy} = Q_{yx} = 10^{-3} rn(\mathbf{r})$ , where  $rn(\mathbf{r})$  is a spatial uniform random number between  $-1$  and  $+1$ ] and 5 mM of ATP distributed on only one side of the system. Then we evolved the fluid flows and ATP distributions for 1,000 units of dimensionless time ( $t^* = 0$ –1,000) with the finite element method using the computational fluid dynamics software COMSOL Multiphysics<sup>TM</sup>.<sup>58</sup>

To test the model's ability to describe the mixing process of an active fluid system with nonuniform activity, we created two simulation systems with the same dimensionless molecular diffusion coefficient of ATP ( $D^* = 16$ ) but one was activated ( $\alpha_0^* = 5$ ) on one side while the other was an inactivated ( $\alpha_0^* = 0$ ) control (Supplementary Video 4). We found that in the control system (Fig. 6a, left column), ATP dispersed only by molecular diffusion, but when the fluid was activated (middle column), active turbulences formed and transported the ATP toward the inactivated region with negligible contribution from molecular diffusion. However, in a third simulation where the ATP molecular diffusion rate was increased ( $D^* = 64$ ), the mixing process sped up (right column). These simulation results show that the process of ATP dispersion is controlled by both molecular diffusion of ATP and active transport; which mechanism dominated the ATP dispersion depended upon the competition between these two mechanisms.

To quantify the efficacy of ATP mixing by active fluid, we analyzed the normalized multiscale norm of ATP concentrations as a function of time<sup>25</sup> for  $\alpha_0^* = 0$ –5 and  $D^* = 1$ –128 (Eq. 5 with  $l = 1$ ). We found that the norms decayed exponentially with time:  $\hat{s} \sim \exp(-t^*/t_0^*)$ , where  $t_0^*$  is the dimensionless mixing time (Fig. 6b), which was consistent with results of Saintillan and Shelley.<sup>25</sup> We then analyzed the mixing time as a function of dimensionless activity level,  $\alpha_0^*$ , for each dimensionless molecular diffusion coefficient  $D^*$  (Fig. 6c). Our analyses revealed that when ATP diffused slowly ( $D^* \lesssim 32$ ), increasing activity level decreased the mixing time monotonically (black to dark purple curves), but as ATP diffused sufficiently fast ( $D^* \gtrsim 64$ ), the mixing time was nearly independent of activity level (purple and magenta curves). Overall, increasing both the molecular diffusion coefficient and the activity level promoted the mixing process and decreased mixing time. Thus, our simulation showed that in a nonuniform activity system, both molecular diffusion and active transport played important roles to disperse and homogenize the suspended components. However, the simulation did not show the transition from active fluid-induced diffusion-like to superdiffusion-like processes (Fig. 6c) that we observed in the experiments (Fig. 5c). This may be due to the lack of consideration of the rheology of microtubule network in our model (see Discussion).

**Mixing efficacy depends on the spatial distribution of activity.** Our experimental and simulated results showed that the mixing process of nonuniform active fluid was different from that of uniform active fluid; however, we had only explored one configuration of nonuniform active fluid system: an activated bulk on one side of a channel adjacent to an inactivated bulk on the other side. To explore how the spatial configuration of activity nonuniformity affects mixing efficacy, we activated active fluid in a checkerboard pattern (Fig. 7a). Like in the previous experiment, 50% of the fluid was activated, but in this case, we used a checkerboard pattern of UV light to split the activated region into smaller cells. This increased the area of the interface where active and inactive fluids could interact. We observed that the checkerboard-patterned

active fluid evolved to a homogeneous state in a shorter period than the system that was only active on one side (1 hour versus 10 hours). To quantify how mixing efficacy was affected by the checkerboard geometry, we monitored how UV-activated fluorescent dyes dispersed from the checkerboard pattern to a uniformly distributed state for checkerboard grid sizes from 1 to 3 mm. We found that the mixing time decreased with decreasing grid size (Fig. 7b). The smaller grid size led to an overall larger active-inactive interface area, which allowed the active fluid to interact with inactive fluid more efficiently. This work demonstrated that the activity distribution played a significant role in the mixing efficacy of active fluid systems.

## Discussion

These results elucidate the self-mixing process of microtubule-kinesin active fluid with nonuniform activity. The mixing process was driven by active transport at the active-inactive interface. When the flow-speed level was low, active transport mixed ATP in a diffusion-like manner (Fig. 2) and the mixing process could be captured with a Fick's law-based model that considered only diffusion as the driving force to disperse ATP (Figs. 3a–3c). The model predicted the consistent scaling of interface progression coefficient, which was consistent with the results from experiments (Fig. 3d). However, the coefficient magnitudes differed by a factor of 5 between the model and the experiments ( $P_{I0} = 2,400 \mu\text{m}^2/\text{s}$  in the model whereas  $P_{I0} = 450 \mu\text{m}^2/\text{s}$  in the experiment). The larger  $P_{I0}$  in the model might be the consequence of two main limitations of the model. First, the model assumes that the caged ATP was fully released upon UV exposure; however, in reality, caged ATP has a limited yield and not every caged ATP molecule becomes usable ATP upon UV exposure. Hence, the model may have overestimated the actual ATP concentration which would cause the model to overestimate  $P_I$ . Second, the model used Michaelis-Menten kinetics (Eq. 4) to convert ATP concentration profiles to mean speed profiles; however, this conversion would overestimate the mean speed profiles at low ATP concentrations,<sup>49</sup> because in low ATP concentration regimes motor dimers are immobile and act as passive crosslinkers in the microtubule network, causing the network to behave like an elastic gel, unlike in networks with high ATP concentrations where motors are mobile and thus the network is fluid.<sup>48,50</sup> Michaelis-Menten kinetics is an enzyme-based model that does not consider network rheology; thus, if the network rheology plays an important role, this conversion would overestimate the flow speed and thus overestimate  $P_I$ . Despite these limitations, this simple model elucidated that the mixing in active-inactive fluid system at low flow-speed levels was governed by a diffusion-like process.

Our results showed that the diffusion-like behaviors of active transport at the active-inactive interface could undergo a transition to superdiffusion-like behaviors as the flow-speed level increased (Figs. 4 & 5c). This is consistent with previous results that showed that tracer motion changed from diffusion-like to superdiffusion-like with increasing activity levels in active fluid.<sup>15,34</sup> However, this transition was not predicted in our active nematohydrodynamic model (Fig. 6c). The transition may be related to the complex rheological properties of the microtubule network, which were absent from our model. At the front of the active-inactive interface, ATP concentrations are low and thus the network can behave like an elastic gel because the inert kinesin motors act as crosslinkers between the microtubules.<sup>50</sup> Behind the front of the interface, where ATP concentrations are higher, the network behaves as a fluid-like network. (Fig. 1c).<sup>48</sup> For the interface to progress, the active network needs to transport ATP to the front of the interface and “melt” the passive network (Supplementary Video 1). When the flow-speed level of the fluid network is low, the ATP transport is slow so the network melting depends mainly on the diffusion-like process of ATP driven by slow active fluid flows at the front of the interface, which leads to slow progression of the interface ( $\gamma \approx 1$ ; Fig. 2). Contrarily, when the flow-speed level is high, ATP quickly piles up at the front of the interface and disperses in a superdiffusion-like manner driven by fast active fluid flows, which quickly melts the network and leads to faster progression of the interface ( $\gamma > 1$ ; Fig. 4). Thus, the progression of the active-inactive fluid interface may be a consequence of the fluid network transporting

ATP molecules to melt the passive network, a process related to the interplay among the ATP dispersion at the interface front (which can be either diffusion-like or superdiffusion-like), ATP transport behind the front (which is constantly superdiffusion-like), and the melting dynamics of the microtubule-kinesin network. Future research to elucidate such a complex interplay could involve monitoring dyes, tracers, and microtubules simultaneously to reveal the correlations among ATP dispersion, fluid flows (active transport), and microtubule network structure (melting). The process could be modeled by introducing ATP-dependent rheological constants to reveal the melting process of the gel-like network at the interface between high and low concentrations of ATP.

The results reported here also demonstrate that the mixing efficacy of the nonuniform active fluid systems depended on the distribution of activity. Systems consisting of more small active areas (high uniformity; e.g., checkerboard-patterned active fluid system [Fig. 7]) evolved to a homogeneous state faster than systems with the same total active area distributed as one piece (low uniformity; e.g., active fluid systems with one side active and one side inactive [Fig. 1c]). This result indicates that the activity-uniform active fluid has the highest mixing performance, and the tendency of nonuniform active fluid evolving toward uniformity is a process of maximizing mixing performance and thus maximizing system entropy (the 2nd law).

This study has other limitations. These experiments focused on the mixing of active and inactive fluids which were two of the same-type fluids except that one was fueled with ATP and the other was unfueled; thus, the results may not be generalizable to active fluids mixing with other types of fluids. Another limitation of this study is that we varied the flow-speed level of active fluid by replacing processive motors with nonprocessive motors and increasing the thickness of sample containers. Both of these methods could change the active fluid properties: replacing processive motors with nonprocessive motors could affect the network rheology<sup>35</sup> and increasing sample thickness could alter the correlation length scale of fluid flows.<sup>38</sup> Thus either strategy might in some way affect mixing efficacy. Future research could investigate how mixing efficacy could be affected by network rheology and sample geometry.

Overall, this work demonstrated that the mixing of nonuniform active fluid systems is fundamentally different from mixing in uniform active fluids. Our findings show that active fluid mixing involves complex interplays among ATP dispersion at the front of the active-inactive interface (which can be either diffusion-like or superdiffusion-like), active transport of ATP behind the front (which is constantly superdiffusion-like), and possibly a fluid-gel transition of the microtubule network,<sup>50</sup> as well as the spatial distribution of activity. This work paves the path to the design of microfluidic devices that use active fluid to internally promote or optimize the micromixing process<sup>10</sup> to enhance production efficiency in chemical and biological engineering and pharmaceutical development.<sup>1</sup> The results will also provide insight into intracellular mixing processes, because the cytoplasmic streaming<sup>59</sup> that supports organelles within cells is powered by cytoskeletal filaments and motor proteins that function similarly to microtubule-kinesin active fluid.<sup>60,61</sup>

## Methods

**Polymerize microtubules.** Microtubules constitute the underlying network of microtubule-kinesin active fluid. The microtubules were polymerized from bovine brain  $\alpha$ - and  $\beta$ -tubulin dimers purified by three cycles of polymerization and depolymerization.<sup>43,62</sup> Microtubules (8 mg/mL) were stabilized with 600  $\mu$ M guanosine-5'[( $\alpha$ , $\beta$ )-methyleno]triphosphate (GMP CPP, Jena Biosciences, NU-4056) and 1 mM dithiothreitol (DTT, Fisher Scientific, AC165680050) in microtubule buffer (80 mM PIPES, 2 mM MgCl<sub>2</sub>, 1 mM ethylene glycol-bis( $\beta$ -aminoethyl ether)-N,N,N',N'-tetraacetic acid, pH 6.8) and polymerized by a 30-minute incubation at 37 °C and a subsequent 6-hour anneal at room temperature before being snap frozen with liquid nitrogen and stored at -80 °C. The microtubules were then labeled with Alexa Fluor 647 (excitation: 650 nm; emission: 671 nm; Invitrogen, A-20006) and mixed with unlabeled microtubules at

3% labeling fraction during polymerization to image microtubules for non-fluorescein experiments (Figs. 1, 2 & 4). For fluorescein experiments, the microtubules were unlabeled (Figs. 5 & 7).

**Dimerize kinesin motor proteins.** Kinesin motor proteins power the extensile motion of sliding microtubule bundle pairs in active fluid by forming a dimer and walking on adjacent antiparallel microtubules to force them in opposite directions (Fig. 1a).<sup>15,63</sup> We expressed kinesin in the *Escherichia coli* derivative Rosetta 2 (DE3) pLysS cells (Novagen, 71403), which we transformed with DNA plasmids from *Drosophila melanogaster* kinesin (DMK) genes.<sup>64</sup> For most experiments in this paper, we used processive motors that include DMK's first 401 N-terminal DNA codons (K401).<sup>65</sup> To explore the effect of low mean speed of active fluid bulk on the interface progression exponent  $\gamma$ , we mixed in fractions of non-processive motors whose plasmid included DMK's first 365 codons (K365, Fig. 4 inset left).<sup>35,49,66</sup> The kinesin motors were tagged with 6 histidines enabling purification via immobilized metal ion affinity chromatography with gravity nickel columns (GE Healthcare, 11003399). To slide adjacent microtubule bundle pairs, kinesin motors needed to be dimerized, so the kinesin motors were tagged with a biotin carboxyl carrier protein at their N terminals, which allowed the kinesins to be bound with biotin molecules (Alfa Aesar, A14207).<sup>15,43</sup> To dimerize the kinesin, we mixed either 1.5  $\mu$ M K401 processive motors or 5.4  $\mu$ M K365 non-processive motors with 1.8  $\mu$ M streptavidin (Invitrogen, S-888) and 120  $\mu$ M DTT in microtubule buffer, incubated them for 30 minutes at 4 °C, and then snap froze them with liquid nitrogen and stored them at –80 °C.

**Prepare microtubule-kinesin active fluid with caged ATP and caged fluorescein.** To prepare the active fluid, we mixed 1.3 mg/mL microtubules with 120 nM kinesin motor dimers and 0.8% polyethylene glycol (Sigma 81300), which acted as a depleting agent to bundle microtubules (Fig. 1a).<sup>15</sup> Kinesin steps from the minus to the plus ends of microtubules by hydrolyzing ATP and producing adenosine diphosphate.<sup>57,67</sup> To control the initial spatial distribution of ATP and thus the activity distribution of active fluid, we used 0.5 to 8 mM caged ATP (adenosine 5'-triphosphate, P3-(1-(4,5-dimethoxy-2-nitrophenyl)ethyl) ester, disodium salt and DMNPE-caged ATP, Fisher Scientific, A1049), which is ATP whose terminal phosphate is esterified with a blocking group rendering it non-hydrolyzable by kinesin motors unless exposed to 360-nm UV light. Exposure to UV light removes the blocking group (Fig. 1b) and allows the kinesin motors to hydrolyze the ATP into ADP and activate the active fluid.<sup>44,45</sup> The ATP hydrolyzation decreased ATP concentrations, which slowed down the kinesin stepping rate and thus decreased active fluid flow speed.<sup>15,34,49,56,57</sup> To maintain ATP concentrations so as to stabilize the activity level of the active fluid bulk over the course of our experiments, we included 2.8% v/v pyruvate kinase/lactate dehydrogenase (Sigma, P-0294), which converted ADP back to ATP.<sup>15,68</sup> To feed the pyruvate kinase enzyme, we added 26 mM phosphoenol pyruvate (BeanTown Chemical, 129745). We imaged the active fluid samples with fluorescent microscopy for 1 to 16 hours, which could bleach the fluorescent dyes and thus decrease the image quality over the course of experiments. To reduce the photobleaching effect, we included 2 mM trolox (Sigma, 238813) and oxygen-scavenging enzymes consisting of 0.038 mg/mL catalase (Sigma, C40) and 0.22 mg/mL glucose oxidase (Sigma, G2133) and fed the enzymes with 3.3 mg/mL glucose (Sigma, G7528).<sup>15</sup> To stabilize proteins in our active fluid system, we added 5.5 mM DTT. To track the fluid flows, we doped the active fluid with 0.0016% v/v fluorescent tracer particles (Alexa 488-labeled [excitation: 499 nm; emission: 520 nm] 3- $\mu$ m polystyrene microspheres, Polyscience, 18861). To test how active fluid could mix suspended components, we introduced 0.5 to 6  $\mu$ M caged, UV-activated fluorescent dyes (fluorescein bis-(5-carboxymethoxy-2-nitrobenzyl) ether, dipotassium salt; CMNB-caged fluorescein, ThermoFisher Scientific, F7103), which is colorless and nonfluorescent until exposed to 360-nm UV light.<sup>44</sup> The dye concentration was chosen to maintain a sufficient signal-to-noise ratio while avoiding brightness saturation in micrographs. Upon UV exposure, the fluorescein became fluorescent and could be observed with fluorescent microscopy; however, the fluorescent spectrum of the fluorescein overlapped with our Alexa

488-labeled tracers, so for our experiments with caged fluorescein (Figs. 5), we replaced the tracers with Flash Red-labeled 2- $\mu$ m polystyrene microspheres (Bangs Laboratories, FSFR005) and used unlabeled microtubules (0% labeling fraction) to prevent fluorescent interference from microtubules while imaging tracers.

**Prepare active-inactive fluid systems.** To prepare the active-inactive fluid system, we loaded the inactivated microtubule-kinesin active fluid with caged ATP to a polyacrylamide-coated glass flow cell ( $20 \times 4 \times 0.1 \text{ mm}^3$ ) with parafilm (Cole-Parmer, EW-06720-40) as a spacer sandwiched between a cover slip (VWR, 48366-227) and slide (VWR, 75799-268)<sup>35</sup> and sealed the channel with epoxy (Bob Smith Industries, BSI-201). Then we masked one side of the sample with a removable mask of opaque black tape (McMaster-Carr, 76455A21) attached to a transparent plastic sheet (Supplementary Fig. 1a) and shined UV light on the sample for 5 minutes before removing the mask (Supplementary Fig. 2). In the unmasked region, the UV light released the ATP from the blocking group and activated the fluid by allowing the ATP to fuel the local kinesin motors; in the masked region, the fluid remained quiescent (Fig. 1c; Supplementary Video 1).<sup>44</sup> To explore how the progression exponent changed with active fluid bulk mean speed, we accelerated fluid flows by making the flow cell thicker by stacking layers of parafilm to decrease hydrodynamic resistance (Fig. 4 inset right).<sup>49,51</sup> To explore how the spatial nonuniformity of activity influenced the mixing efficacy of the active-inactive fluid system, we masked the sample with checkerboard-patterned masks (FineLine Imaging, Fig. 7).

**Image samples with dual fluorescent channels.** We imaged the active fluids with epifluorescent microscopy (Ti2-E Inverted Microscope, Nikon, MEA54000). To capture a wide area of the sample ( $20 \times 4 \text{ mm}^2$ ), we used a 4 $\times$  objective lens (CFI Plan Apo Lambda 4 $\times$  Obj, Nikon, MRD00045, NA 0.2) to image 3 to 4 adjacent frames rapidly ( $\lesssim 3 \text{ s}$ ) and stitched the micrographs into one large image for flow and dye dispersion analyses (Figs. 1, 2, 4, 5, and 7; Supplementary Fig. 1b).

Performing these analyses required monitoring at least two components in two fluorescent channels in each sample; for example, the dye dispersion experiments (Fig. 5) required analyzing fluorescent dyes (excitation: 490 nm; emission: 525nm) and Flash Red-labeled tracers (excitation: 660 nm; emission: 690 nm) simultaneously. This could have been accomplished by programming a microscope to rapidly switch back and forth between filter cubes, but this would have quickly worn down the turret motor. Additionally the time required to switch filter cubes ( $\gtrsim 4 \text{ s}$ ), added to the time involved in moving the stage to capture adjacent images and stitching them ( $\sim 3 \text{ s}$ ), would have made the minimum time interval between frames  $\gtrsim 10 \text{ s}$ , which would have prevented us from tracking high-density tracers ( $1000 \text{ mm}^{-3}$  with a mean separation of 5  $\mu\text{m}$  in a 0.1-mm-thick sample) whose speeds were 1 to 10  $\mu\text{m/s}$ , even with a predictive Lagrangian tracking algorithm.<sup>69</sup>

To overcome this technical challenge in imaging our samples, we established a dual-channel imaging system that consisted of a multiband pass filter cube (Multi LED set, Chroma, 89402-ET) and voltage trigger (Nikon) placed between the light source (pE-300<sup>ultra</sup>, CoolLED, BU0080) and camera (Andor Zyla, Nikon, ZYLA5.5-USB3). Instead of changing filter cubes, the multiband pass filter cube allowed us to switch between multiple emission bands and excitation bands by switching between channels with the same filter cube (Supplementary Fig. 3). We alternatively activated the blue (401–500 nm) and red (500–700 nm) LEDs to excite and observe the fluorescent dyes and tracers almost simultaneously. The LED light source communicated directly with the camera via voltage triggering to coordinate LED activation time and bypass computer control to further boost the light switching rate. This technique shortened our channel switching time to 3 to 5  $\mu\text{s}$ ; thus the time interval between image acquisitions of different fluorescent channels was only limited by exposure times of each channel. This setup allowed us to image two fluorescent channels almost simultaneously (within milliseconds) and thus enabled us to monitor two fluorescent components

side-by-side such as microtubules and tracers (Fig. 1c; Supplementary Video 1), caged fluorescent dyes and tracers (Fig. 5c), and caged fluorescent dyes and microtubules (Supplementary Video 5).

**Analyze positions of active-inactive fluid interfaces.** We characterized the mixing kinematics of active and inactive fluids by analyzing the interface progression exponents  $\gamma$  and coefficients  $P_I$  (Figs. 2–4). These analyses required identification of the interface positions. We determined the interface positions by first tracking tracers in sequential images with the Lagrangian tracking algorithm,<sup>69</sup> which revealed the tracers' trajectories  $r_i(t)$  and corresponding instantaneous velocities  $v_i \equiv dr_i/dt$ . Then we analyzed the speed profile of tracers by binning the tracer speed  $|v_i|$  across the width of the channel  $S(x_j) \equiv \langle |v_i| \rangle_{i \in \text{bin } j}$  where  $x_j$  was the horizontal  $x$  coordinate of the  $j$ th bin and the  $\langle |v_i| \rangle_{i \in \text{bin } j}$  represented the average speed of tracers in the  $j$ th bin. Then we normalized the speed profile by rescaling the speed profile to be 1 in the active zone and 0 in the inactive zone:  $S^*(x) \equiv [S(x) - s_{in}]/[s_a - s_{in}]$ , where  $s_a$  was the average of speed profiles in the active zone and  $s_{in}$  was the average of speed profiles in the inactive zone (Fig. 1e). Then we defined the width of the active-inactive fluid interface as where the normalized speed profile was between 0.2 and 0.8 (dashed lines in Fig. 1e inset) and the position of the interface  $x_I$  as where the normalized speed profile was 0.5 (solid line). The interface position was then analyzed for each frame, which allowed us to determine the interface displacement,  $\Delta x \equiv x_I(\Delta t) - x_I(0)$ , versus time lapse,  $\Delta t$  (Fig. 2a inset), and the squared interface displacement,  $\Delta x^2$ , versus time lapse,  $\Delta t$  (Fig. 2a). To determine the interface progression exponent  $\gamma$ , we fit  $\log(\Delta x^2)$  versus  $\log(\Delta t)$  data to  $\log(\Delta x^2) = \log(2P_I) + \gamma \log(\Delta t)$ , with  $P_I$  and  $\gamma$  as fitting parameters (Figs. 2b & 4). To determine the interface progression coefficient  $P_I$ , we assumed  $\gamma = 1$  and fit  $\Delta x^2$  versus  $\Delta t$  data to  $\Delta x^2 = 2P_I\Delta t$  with  $P_I$  as the fitting parameter (Figs. 2c, 3c & 3d).

**Generate flow speed map of active-inactive fluid system with particle image velocimetry algorithm.** To visualize the activity distribution in our active-inactive fluid system, we analyzed the distribution of flow speed to generate flow speed maps (Fig. 1d). To complete this analysis, we analyzed the flow velocities of fluids by analyzing the tracer motions in sequential images with a particle image velocimetry algorithm,<sup>70</sup> which revealed the flow velocity field  $\mathbf{V}(\mathbf{r}, t)$  and associated distribution of flow speed  $|\mathbf{V}(\mathbf{r}, t)|$  in each frame. A heat color bar was used to plot the speed distributions into color maps to reveal the evolution of speed distribution from the pre-activated state (black) to the homogeneously activated state (red/yellow) (Fig. 1d).

**Numerically solve the Fick's law equations.** We modeled diffusion-dominated active-inactive fluid mixing with the Fick's law equation, which required us to solve for the concentration of ATP (Eq. 1). To simplify the modeling, we considered only one-dimensional active fluid system confined in a segment  $x = 0-L$  where  $L = 20$  mm, the length of our experimental sample. Given that ATP is confined in the segment, we applied no-flux boundary conditions to the ATP concentrations (Eq. 2). In the experiment, we exposed the left side of the sample to UV light to release ATP, so in our model the ATP concentration has a step function as its initial condition (Eq. 3). With the initial condition and boundary conditions, we solved the Fick's law equation to determine the spatial and temporal distribution of ATP. We used Mathematica 13.0 to numerically solve this differential equation with the NDSolveValue function by feeding Eqs. 1–3 into the function followed by specifying the spatial and temporal domains, which output the numerical solution of ATP concentration  $C(x, t)$  and allowed us to determine the evolution of ATP distribution (Fig. 3a). Then we converted the ATP distribution to mean speed distribution of active fluid by the Michaelis-Menten kinetics (Eq. 4; Fig. 3b inset), which showed a uniform mean speed in the left side of the sample followed by gradual activation of the right side of the system until a uniform state was reached (Fig. 3b). Then we defined the position of the active-inactive fluid interface  $\Delta x$  as where the mean speed decayed to a half (Fig. 3c inset), which allowed us to plot the squared interface displacement as a function of time (Fig. 3c). The plot in log-log axes exhibited a line with a unit slope, which suggested that the squared interface

displacement is linearly proportional to time. By assuming this linear relation, we determined the interface progression coefficient  $P_I$  by fitting  $\Delta x^2 = 2P_I\Delta t$  with  $P_I$  as the fitting parameter. Finally, we repeated the calculation with different initial ATP concentrations in the left side of the system,  $C_0$ , and plotted the normalized interface progression coefficient  $P_I/P_{I0}$  as a function of  $C_0$  where  $P_{I0}$  is the progression coefficient when the initial ATP concentration is 8 mM. This plot allowed us to compare the simulation results with the experimental measurements to examine the validity of our Fick's law-based model (Fig. 3d).

**Numerically solve the active nematohydrodynamic equations in weak forms.** To model the mixing of active and inactive fluids, we adopted Varghese *et al.*'s active fluid model to include the dynamics of the ATP concentration field.<sup>22</sup> Our model had four main components: (1) the kinetic equation describing the kinematics of self-elongating rods that flow and orient with the solvent as well as diffuse translationally and rotationally (Eq. 6), (2) the Stokes equation describing how the solvent was driven by the active stress exerted by the self-elongating rods (Eq. 7), (3) the relationship between  $\alpha$  and ATP that describes how the active stress depended on the nonuniform ATP distribution (Eq. 8), and (4) the continuity equation of ATP transport that describes how ATP diffuses as well as flows with the solvent (Eq. 10). We numerically solved these coupled equations with appropriate boundary and initial conditions using the finite element method by first converting them to their weak forms and then implementing them symbolically in COMSOL Multiphysics<sup>TM</sup>.<sup>58</sup> We show below the weak form of the convection-diffusion equation governing the evolution of ATP concentration field:

$$\int_{\Gamma} dx^* dy^* \tilde{T} \frac{\partial C}{\partial t^*} = - \int_{\Gamma} dx^* dy^* D^* \left( \frac{\partial \tilde{T}}{\partial x^*} \frac{\partial C}{\partial x^*} + \frac{\partial \tilde{T}}{\partial y^*} \frac{\partial C}{\partial y^*} \right) - \int_{\Gamma} dx^* dy^* \tilde{T} \left( u_x^* \frac{\partial C}{\partial x^*} + u_y^* \frac{\partial C}{\partial y^*} \right), \quad 11$$

where  $\tilde{T}(x^*, y^*)$  is the test function and  $\Gamma$  represents the system spatial domain. After solving these equations, we determined the spatial and temporal distributions of ATP concentrations and active fluid flow speeds (Fig. 6a and Supplementary Video 4), which allowed us to explore how the activity level of active fluid and molecular diffusion of ATP influenced the mixing process of ATP in nonuniform active fluid systems (Figs. 6b & c).

**Data availability:** The data that support the findings of this study are available from the corresponding author upon reasonable request.

## References

- 1 Jeong, G. S., Chung, S., Kim, C.-B. & Lee, S.-H. Applications of micromixing technology. *Analyst* **135**, 460-473 (2010).
- 2 Haswell, S. J. *et al.* The application of micro reactors to synthetic chemistry. *Chemical Communications*, 391-398 (2001).
- 3 Hadd, A. G., Raymond, D. E., Halliwell, J. W., Jacobson, S. C. & Ramsey, J. M. Microchip device for performing enzyme assays. *Analytical Chemistry* **69**, 3407-3412 (1997).
- 4 Kakuta, M., Jayawickrama, D. A., Wolters, A. M., Manz, A. & Sweedler, J. V. Micromixer-based time-resolved NMR: Applications to ubiquitin protein conformation. *Analytical Chemistry* **75**, 956-960 (2003).
- 5 Lian, Y. & Shyy, W. Laminar-turbulent transition of a low Reynolds number rigid or flexible airfoil. *AIAA Journal* **45**, 1501-1513 (2007).
- 6 Ottino, J. M. Mixing, chaotic advection, and turbulence. *Annual Review of Fluid Mechanics* **22**, 207-254 (1990).
- 7 Suzuki, H., Chih-Ming, H. & Kasagi, N. A chaotic mixer for magnetic bead-based micro cell sorter. *Journal of Microelectromechanical Systems* **13**, 779-790 (2004).
- 8 Liu, R. H., Yang, J., Pindera, M. Z., Athavale, M. & Grodzinski, P. Bubble-induced acoustic micromixing. *Lab on a Chip* **2**, 151-157 (2002).
- 9 Groisman, A. & Steinberg, V. Efficient mixing at low Reynolds numbers using polymer additives. *Nature* **410**, 905-908 (2001).
- 10 Ober, T. J., Foresti, D. & Lewis, J. A. Active mixing of complex fluids at the microscale. *Proceedings of the National Academy of Sciences* **112**, 12293-12298 (2015).
- 11 Barbic, M., Mock, J. J., Gray, A. P. & Schultz, S. Electromagnetic micromotor for microfluidics applications. *Applied Physics Letters* **79**, 1399-1401 (2001).
- 12 Ramaswamy, S. Active fluids. *Nature Reviews Physics* **1**, 640-642 (2019).
- 13 Sokolov, A., Apodaca, M. M., Grzybowski, B. A. & Aranson, I. S. Swimming bacteria power microscopic gears. *Proceedings of the National Academy of Sciences* **107**, 969-974 (2010).
- 14 Lushi, E., Wioland, H. & Goldstein, R. E. Fluid flows created by swimming bacteria drive self-organization in confined suspensions. *Proceedings of the National Academy of Sciences* **111**, 9733-9738 (2014).
- 15 Sanchez, T., Chen, D. T. N., DeCamp, S. J., Heymann, M. & Dogic, Z. Spontaneous motion in hierarchically assembled active matter. *Nature* **491**, 431-434 (2012).
- 16 Palacci, J., Sacanna, S., Steinberg, A. P., Pine, D. J. & Chaikin, P. M. Living crystals of light-activated colloidal surfers. *Science* **339**, 936-940 (2013).
- 17 Soni, V. *et al.* The odd free surface flows of a colloidal chiral fluid. *Nature Physics* **15**, 1188 (2019).
- 18 Marchetti, M. C. *et al.* Hydrodynamics of soft active matter. *Reviews of Modern Physics* **85**, 1143-1189 (2013).
- 19 Gompper, G. *et al.* The 2020 motile active matter roadmap. *Journal of Physics: Condensed Matter* **32**, 193001 (2020).
- 20 Needleman, D. & Dogic, Z. Active matter at the interface between materials science and cell biology. *Nature Reviews Materials* **2**, 17048 (2017).
- 21 Thampi, S. P. & Yeomans, J. M. Active turbulence in active nematics. *The European Physical Journal Special Topics* **225**, 651-662 (2016).
- 22 Dunkel, J. *et al.* Fluid dynamics of bacterial turbulence. *Physical Review Letters* **110**, 228102 (2013).
- 23 Wensink, H. H. *et al.* Meso-scale turbulence in living fluids. *Proceedings of the National Academy of Sciences* **109**, 14308-14313 (2012).
- 24 Tan, A. J. *et al.* Topological chaos in active nematics. *Nature Physics* **15**, 1033-1039 (2019).
- 25 Saintillan, D. & Shelley, M. J. Instabilities, pattern formation, and mixing in active suspensions. *Physics of Fluids* **20**, 123304 (2008).

26 Kim, M. J. & Breuer, K. S. Enhanced diffusion due to motile bacteria. *Physics of Fluids* **16**, L78-L81 (2004).

27 del Junco, C., Estevez-Torres, A. & Maitra, A. Front speed and pattern selection of a propagating chemical front in an active fluid. *Physical Review E* **105**, 014602 (2022).

28 Vyborna, Y., Galas, J.-C. & Estevez-Torres, A. DNA-controlled spatiotemporal patterning of a cytoskeletal active gel. *Journal of the American Chemical Society* **143**, 20022-20026 (2021).

29 Wysocki, A., Winkler, R. G. & Gompper, G. Propagating interfaces in mixtures of active and passive Brownian particles. *New Journal of Physics* **18**, 123030 (2016).

30 Blow, M. L., Thampi, S. P. & Yeomans, J. M. Biphasic, lyotropic, active nematics. *Physical Review Letters* **113**, 248303 (2014).

31 Ross, T. D. *et al.* Controlling organization and forces in active matter through optically defined boundaries. *Nature* **572**, 224-229 (2019).

32 Zhang, R. *et al.* Spatiotemporal control of liquid crystal structure and dynamics through activity patterning. *Nature Materials* **20**, 875-882 (2021).

33 Shankar, S. & Marchetti, M. C. Hydrodynamics of active defects: From order to chaos to defect ordering. *Physical Review X* **9**, 041047 (2019).

34 Henkin, G., DeCamp, S. J., Chen, D. T. N., Sanchez, T. & Dogic, Z. Tunable dynamics of microtubule-based active isotropic gels. *Philosophical Transactions. Series A, Mathematical, Physical, and Engineering Sciences* **372**, 20140142 (2014).

35 Chandrakar, P. *et al.* Engineering stability, longevity, and miscibility of microtubule-based active fluids. *Soft Matter* **18**, 1825-1835 (2022).

36 Tayar, A. M., Hagan, M. F. & Dogic, Z. Active liquid crystals powered by force-sensing DNA-motor clusters. *Proceedings of the National Academy of Sciences* **118**, e2102873118 (2021).

37 Duclos, G. *et al.* Topological structure and dynamics of three-dimensional active nematics. *Science* **367**, 1120-1124 (2020).

38 Fan, Y., Wu, K.-T., Aghvami, S. A., Fraden, S. & Breuer, K. S. Effects of confinement on the dynamics and correlation scales in kinesin-microtubule active fluids. *Physical Review E* **104**, 034601 (2021).

39 Lemma, L. M. *et al.* Multiscale microtubule dynamics in active nematics. *Physical Review Letters* **127**, 148001 (2021).

40 Gao, T., Blackwell, R., Glaser, M. A., Betterton, M. D. & Shelley, M. J. Multiscale polar theory of microtubule and motor-protein assemblies. *Physical Review Letters* **114**, 048101 (2015).

41 Thampi, S. P., Golestanian, R. & Yeomans, J. M. Vorticity, defects and correlations in active turbulence. *Philosophical Transactions of the Royal Society A: Mathematical, Physical and Engineering Sciences* **372**, 20130366 (2014).

42 Doostmohammadi, A., Ignés-Mullol, J., Yeomans, J. M. & Sagués, F. Active nematics. *Nature Communications* **9**, 3246 (2018).

43 Bate, T. E., Jarvis, E. J., Varney, M. E. & Wu, K.-T. Controlling flow speeds of microtubule-based 3D active fluids using temperature. *Journal of Visualized Experiments*, e60484 (2019).

44 Berezney, J., Goode, B. L., Fraden, S. & Dogic, Z. Extensile to contractile transition in active microtubule-actin composites generates layered asters with programmable lifetimes. *Proceedings of the National Academy of Sciences* **119**, e2115895119 (2022).

45 McCray, J. A., Herbette, L., Kihara, T. & Trentham, D. R. A new approach to time-resolved studies of ATP-requiring biological systems; laser flash photolysis of caged ATP. *Proceedings of the National Academy of Sciences* **77**, 7237-7241 (1980).

46 Bowen, W. J. & Martin, H. L. The diffusion of adenosine triphosphate through aqueous solutions. *Archives of biochemistry and biophysics* **107**, 30-36 (1964).

47 Chen, Y.-C., Jolicoeur, B., Chueh, C.-C. & Wu, K.-T. Flow coupling between active and passive fluids across water-oil interfaces. *Scientific Reports* **11**, 13965 (2021).

48 Gagnon, D. A. *et al.* Shear-induced gelation of self-yielding active networks. *Physical Review Letters* **125**, 178003 (2020).

49 Bate, T. E., Jarvis, E. J., Varney, M. E. & Wu, K.-T. Collective dynamics of microtubule-based 3D active fluids from single microtubules. *Soft Matter* **15**, 5006-5016 (2019).

50 Najma, B. *et al.* Dual antagonistic role of motor proteins in fluidizing active networks. *arXiv:2112.11364 [cond-mat.soft]*. (2021).

51 Wu, K.-T. *et al.* Transition from turbulent to coherent flows in confined three-dimensional active fluids. *Science* **355**, eaal1979 (2017).

52 Varghese, M., Baskaran, A., Hagan, M. F. & Baskaran, A. Confinement-induced self-pumping in 3D active fluids. *Physical Review Letters* **125**, 268003 (2020).

53 Aditi Simha, R. & Ramaswamy, S. Hydrodynamic fluctuations and instabilities in ordered suspensions of self-propelled particles. *Physical Review Letters* **89**, 058101 (2002).

54 Guillamat, P., Hardouin, J., Prat, B. M., Ignés-Mullol, J. & Sagués, F. Control of active turbulence through addressable soft interfaces. *Journal of Physics: Condensed Matter* **29**, 504003 (2017).

55 Lemma, L. M., Decamp, S. J., You, Z., Giomi, L. & Dogic, Z. Statistical properties of autonomous flows in 2D active nematics. *Soft Matter* **15**, 3264 (2019).

56 Coy, D. L., Wagenbach, M. & Howard, J. Kinesin takes one 8-nm step for each ATP that it hydrolyzes. *Journal of Biological Chemistry* **274**, 3667-3671 (1999).

57 Schnitzer, M. J. & Block, S. M. Kinesin hydrolyses one ATP per 8-nm step. *Nature* **388**, 386-390 (1997).

58 Bendaraa, A., Charafi, M. M. & Hasnaoui, A. Numerical study of natural convection in a differentially heated square cavity filled with nanofluid in the presence of fins attached to walls in different locations. *Physics of Fluids* **31**, 052003 (2019).

59 Serbus, L. R., Cha, B.-J., Theurkauf, W. E. & Saxton, W. M. Dynein and the actin cytoskeleton control kinesin-driven cytoplasmic streaming in *Drosophila* oocytes. *Development* **132**, 3743-3752 (2005).

60 Woodhouse, F. G. & Goldstein, R. E. Cytoplasmic streaming in plant cells emerges naturally by microfilament self-organization. *Proceedings of the National Academy of Sciences* **110**, 14132-14137 (2013).

61 Suzuki, K., Miyazaki, M., Takagi, J., Itabashi, T. & Ishiwata, S. i. Spatial confinement of active microtubule networks induces large-scale rotational cytoplasmic flow. *Proceedings of the National Academy of Sciences* **114**, 2922-2927 (2017).

62 Castoldi, M. & Popov, A. V. Purification of brain tubulin through two cycles of polymerization-depolymerization in a high-molarity buffer. *Protein Expression and Purification* **32**, 83-88 (2003).

63 Ndlec, F. J., Surrey, T., Maggs, A. C. & Leibler, S. Self-organization of microtubules and motors. *Nature* **389**, 305-308 (1997).

64 Baneyx, F. Recombinant protein expression in *Escherichia coli*. *Current Opinion in Biotechnology* **10**, 411-421 (1999).

65 Martin, D. S., Fathi, R., Mitchison, T. J. & Gelles, J. FRET measurements of kinesin neck orientation reveal a structural basis for processivity and asymmetry. *Proceedings of the National Academy of Sciences* **107**, 5453-5458 (2010).

66 Young, E. C., Mahtani, H. K. & Gelles, J. One-headed kinesin derivatives move by a nonprocessive, low-duty ratio mechanism unlike that of two-headed kinesin. *Biochemistry* **37**, 3467-3479 (1998).

67 Vale, R. D. & Milligan, R. A. The way things move: looking under the hood of molecular motor proteins. *Science* **288**, 88-95 (2000).

68 Chen, Daniel T. N., Heymann, M., Fraden, S., Nicastro, D. & Dogic, Z. ATP consumption of eukaryotic flagella measured at a single-cell level. *Biophysical Journal* **109**, 2562-2573 (2015).

69 Ouellette, N. T., Xu, H. & Bodenschatz, E. A quantitative study of three-dimensional Lagrangian particle tracking algorithms. *Experiments in Fluids* **40**, 301-313 (2005).

70 Thielicke, W. & Stamhuis, E. J. PIVlab—towards user-friendly, affordable and accurate digital particle image velocimetry in MATLAB. *Journal of Open Research Software* **2**, e30 (2014).

## Acknowledgements

T.E.B. and K.-T.W. would like to thank Drs. Seth Fraden and Aparna Baskaran of Brandeis University for insightful discussions on experiments and modeling in this manuscript. T.E.B. and K.-T.W. would also like to thank Dr. John Berezney of Brandeis University for assisting us in developing the UV light setup (Supplementary Fig. 2). T.E.B., E.H.T., and K.-T.W. acknowledge support from the National Science Foundation (NSF-CBET-2045621). This research was performed with computational resources supported by the Academic & Research Computing Group at Worcester Polytechnic Institute. We acknowledge the Brandeis Materials Research Science and Engineering Center (NSF-MRSEC-DMR-2011846) for use of the Biological Materials Facility. Parts of the work by C.-C. C. were funded and supported through the 2022 Early Career Award from the College of Engineering and the Headquarters of University Advancement at National Cheng Kung University, which was sponsored by the Ministry of Education, Taiwan. M.M.N. was supported by the U.S. Department of Energy, Office of Science, Office of Basic Energy Sciences under Award No. DE-SC0022280.

## Author Contributions

T.E.B., M.E.V., and K.-T.W. performed the research and designed the experiments; M.E.V. initiated the experiments; T.E.B., M.E.V., E.H.T. and J.H.D. collected experimental data; T.E.B., M.E.V., and K.-T.W. organized and analyzed the data; T.E.B., E.H.T., C.-C.C., M.M.N. and K.-T.W. established the continuum simulation platform on modeling nonuniform active fluid systems; T.E.B. and K.-T.W. wrote the manuscript; and K.-T.W. supervised the research. All authors reviewed the manuscript.

## Additional Information

**Competing interests statement.** The authors declare that they have no competing interests.

**Correspondence.** Correspondence and requests for materials should be addressed to K.-T.W. ([kwu@wpi.edu](mailto:kwu@wpi.edu)). Active fluid simulation questions should be addressed to C.-C.C. ([chuehcc@mail.ncku.edu.tw](mailto:chuehcc@mail.ncku.edu.tw)), M.M.N. ([mmnsps@rit.edu](mailto:mmnsps@rit.edu)), and K.-T.W. ([kwu@wpi.edu](mailto:kwu@wpi.edu)).

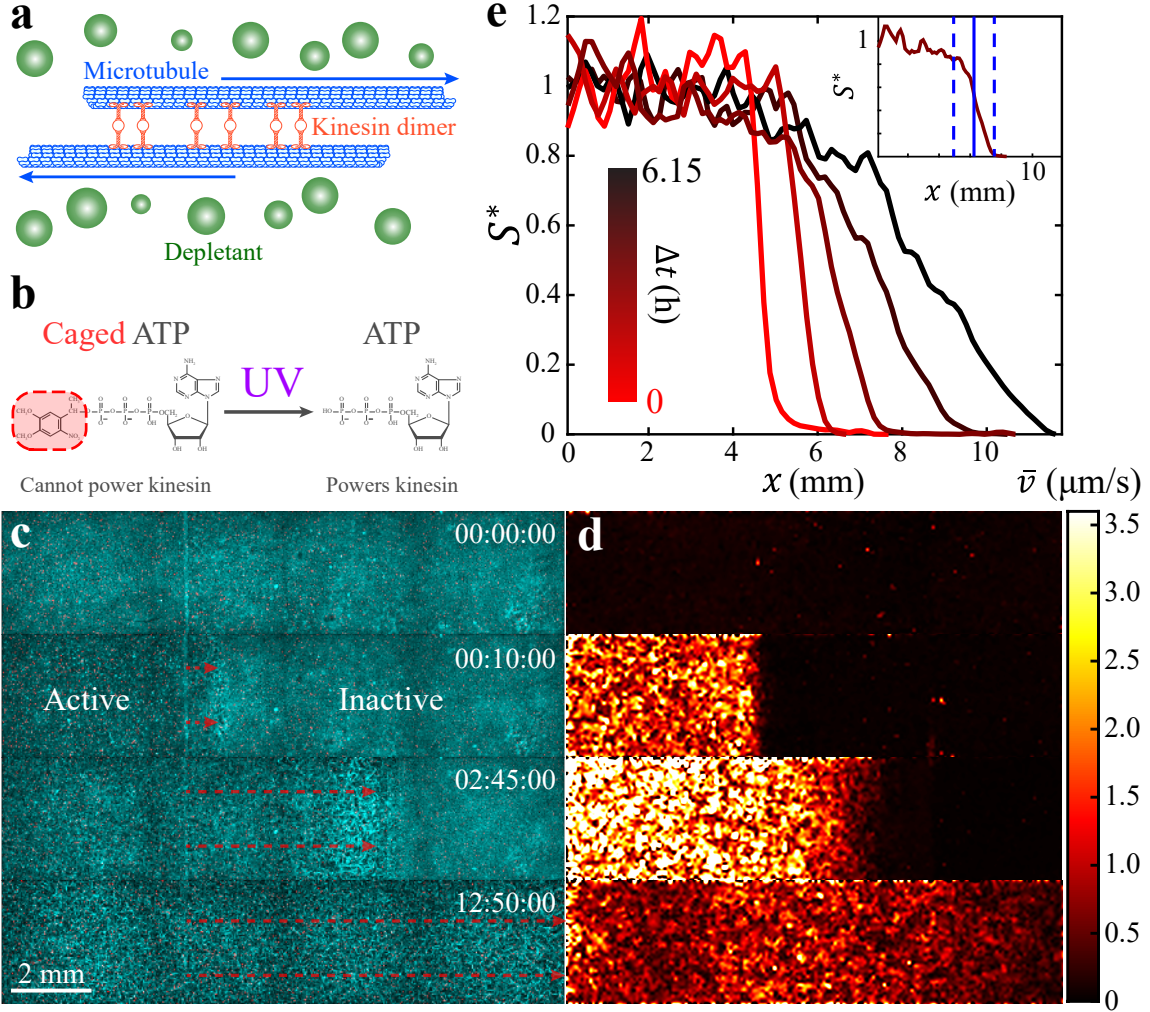


Fig. 1: Mixing of activated and inactivated microtubule-kinesin active fluid. (a) Schematic of microscopic dynamics in microtubule-kinesin active fluid. Depletants force microtubules into bundles that can be bridged by kinesin motor dimers. The kinesin motors “walk” along the microtubules, forcing them to slide apart. The collective sliding dynamics cause the microtubules to form an extensible microtubule network that stirs the surrounding solvents and causes millimeter-scale chaotic flows.<sup>15</sup> (b) Molecular structure of caged ATP. Caged ATP is not hydrolysable by kinesin motors. When caged ATP is exposed to ultraviolet light, the ATP is released and activates the active fluid.<sup>44,45</sup> (c) We saturated a channel of microtubule-kinesin mixture with caged ATP and exposed only one side of the sample to ultraviolet light, which released the ATP and activated the microtubule-kinesin mixture on that side of the channel. The released ATP dispersed toward the unexposed region, which activated the inactive fluid and expanded the active region until the system reached the activity-homogeneous state. Due to the limited speed of multi-position imaging, only one quarter of the active region was imaged (Supplementary Fig. 1b; Supplementary Video 1). (d) Tracking tracer particles revealed the speed distribution of fluid flows, showing the initiation and propagation of the active region into the inactive region. (e) Binning the same-time speeds vertically across the interface of active and inactive fluids revealed the speed profile  $S$  which was normalized as  $S^*(x) \equiv [S(x) - s_{in}]/[s_a - s_{in}]$ , where  $s_a$  was the average of speed profiles in the active zone and  $s_{in}$  was the average of speed profiles in the inactive zone. Inset: The interface of the active and inactive fluids was determined as the region where the normalized speed profile was between 0.2 and 0.8 (dashed blue lines). The position of the interface was determined as where the normalized speed profile was 0.5 (solid blue line).

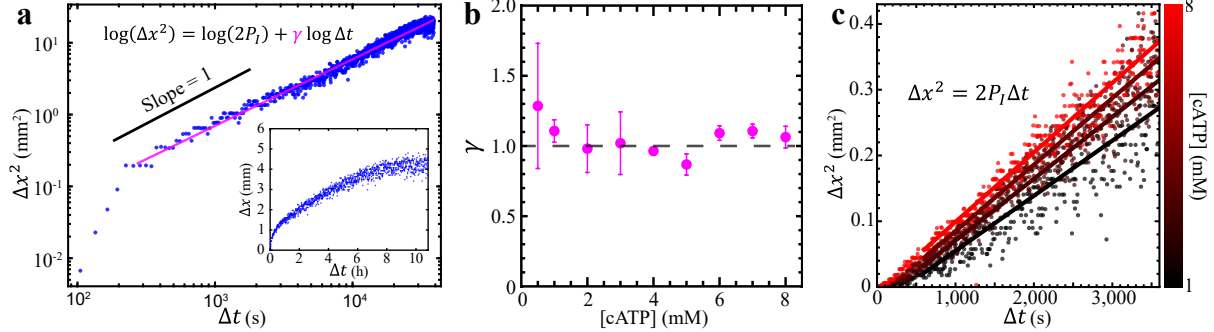


Fig. 2: The progression of the active-inactive interface was governed by diffusion-like process of ATP at the interface, disregarding caged ATP concentrations. (a) Squared interface displacement ( $\Delta x^2$ ) as a function of time ( $\Delta t$ ) revealed a long-term ( $\Delta t \gtrsim 200$  s) linear relation between  $\Delta x^2$  and  $\Delta t$ :  $\Delta x^2 \sim \Delta t^\gamma$  with the interface progression exponent  $\gamma \approx 1$ . Inset: The interface displacement versus time showed that the interface moved rapidly initially and then gradually slowed down. (b) The interface progression exponent was  $\gamma \approx 1$  on average and was independent of the caged ATP concentration. Each error bar represents the standard deviation of  $\geq 3$  trials. (c) Selected examples of squared interface displacement versus time for four caged ATP concentrations from 1 (black) to 8 (red) mM. The motility of the interface was characterized with an interface progression coefficient  $P_I$  determined by fitting the  $\Delta x^2$  versus  $\Delta t$  data to  $\Delta x^2 = 2P_I\Delta t$  with  $P_I$  as the fitting parameter (colored lines). Increasing caged ATP concentrations increased interface progression coefficient (steeper fit lines from black to red) indicating a more motile interface at a higher caged ATP concentration.

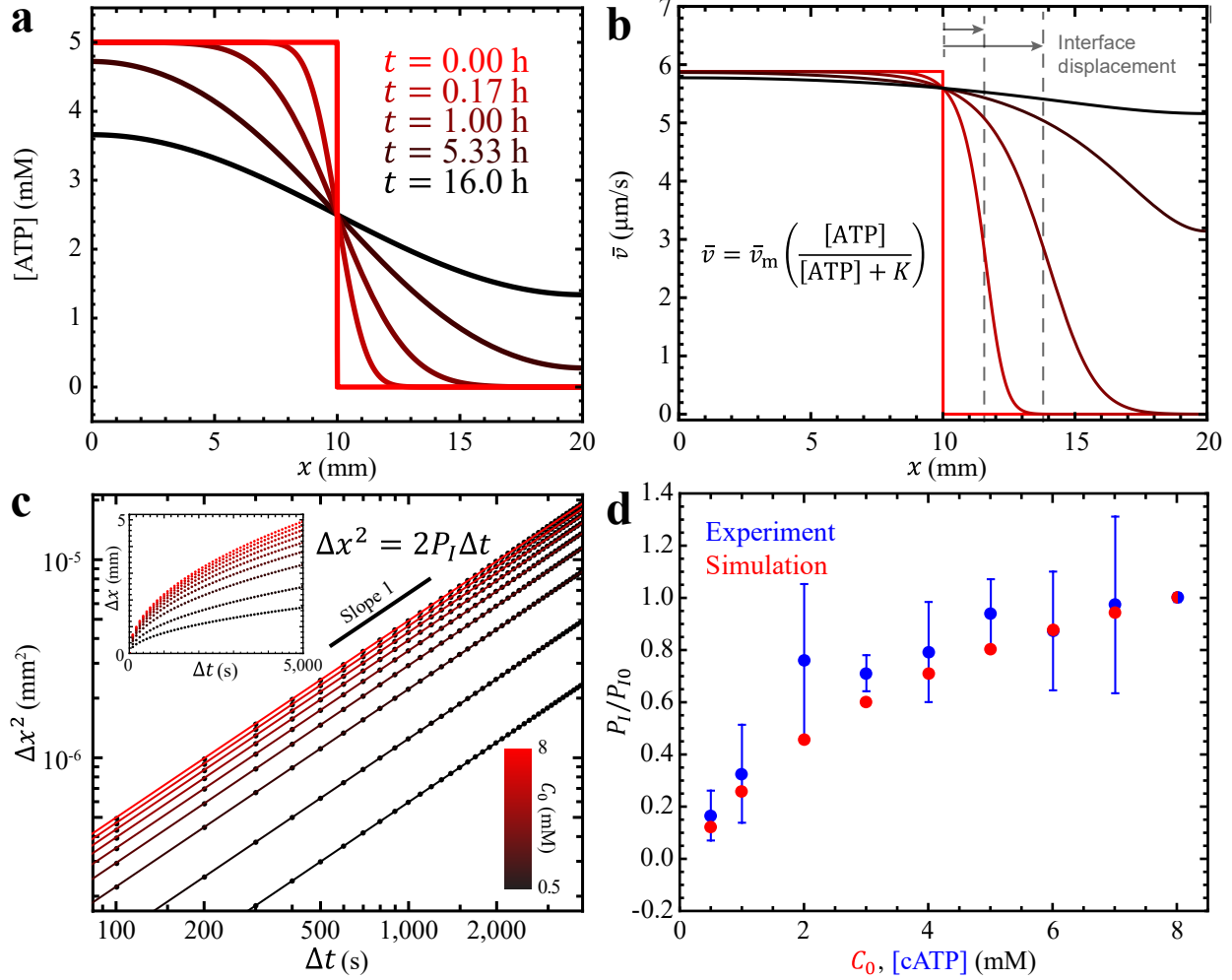


Fig. 3: Fick's law of diffusion and Michaelis-Menten kinetics captured the diffusion-like mixing between active and inactive fluids. (a) The distribution of ATP concentrations started as a step function (red,  $t = 0$  h) and then developed into a smoothed hill function (black,  $t = 16$  h) as ATP evolved from a one-sided distributed to a homogeneous state. (b) The ATP distribution was converted to speed distribution of active fluid via Michaelis-Menten kinetics:  $\bar{v} = \bar{v}_m \left[ \frac{[ATP]}{[ATP] + K} \right]$ , where  $\bar{v}_m = 6.2 \mu\text{m/s}$  and  $K = 270 \mu\text{M}$  (based on our previous studies<sup>49</sup>). The corresponding mean speed distribution of active fluid evolved from a step function distribution (red,  $t = 0$  h) to a near-constant function (black,  $t = 16$  h) (Supplementary Video 2). (c) The diffusion-driven mixing process led the squared interface displacement to be proportional to time, regardless of initial ATP concentration  $C_0$ . Inset: Interface displacement increased rapidly with time initially followed by a gradual deceleration similar to the experimental observation (Fig. 2a inset). (d) The normalized interface progression coefficient  $P_I/P_{I0}$  increased with the initial concentration of ATP,  $C_0$  (or caged ATP concentration for experiments) where  $P_{I0}$  was the interface progression coefficient at  $C_0 = 8 \text{ mM}$  (or  $[\text{cATP}] = 8 \text{ mM}$  for experiments) which was  $P_{I0} = 2,400 \mu\text{m}^2/\text{s}$  for the model and  $P_{I0} = 450 \mu\text{m}^2/\text{s}$  for the experiment. The normalized interface progression coefficient  $P_I/P_{I0}$  in the model (red dots) scaled consistently with the one in the experiment (blue dots). Each error bar in the blue dot represents the standard deviation of  $\geq 3$  trials.

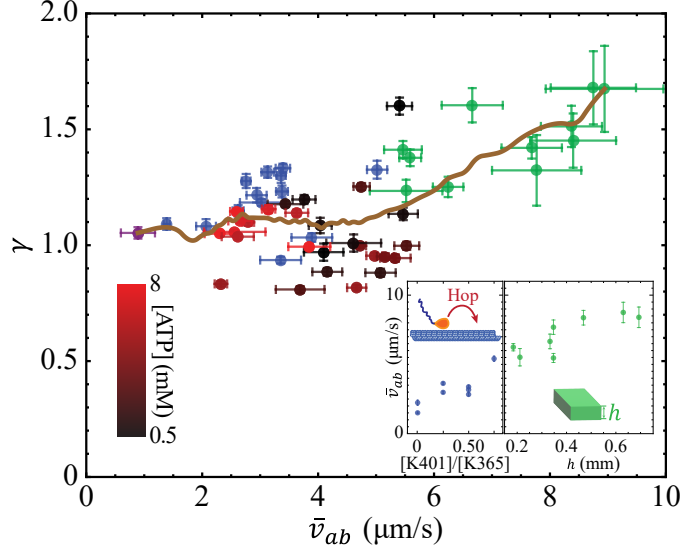


Fig. 4: The interface progression exponent ( $\gamma$ ) increased with the flow-speed level of the active fluid ( $\bar{v}_{ab}$ ). Shown are data from experiments with low ATP concentration (0.5 mM, black dots), high ATP concentration (8 mM, red dots) (Fig. 2b), decreased flow speeds from partially replacing processive motors with non-processive motors (blue dots), increased flow speeds from increasing sample thickness (green dots),<sup>49</sup> and both introducing non-processive motors and increasing sample thickness (purple dot). The brown curve represents the moving average of  $\gamma$ . While the analyzed  $\gamma$  from each experiment was noisy, the moving averaged  $\gamma$  exhibited an overall monotonic increase with the flow-speed level of active fluid  $\bar{v}_{ab}$ . Each dot represents one experimental measurement. Each error bar in  $\gamma$  represents the slope fitting error in  $\ln \Delta x^2 = \ln(2P_f) + \gamma \ln \Delta t$  (Fig. 2a) and each error bar in  $\bar{v}_{ab}$  represents the standard deviation of flow speeds in the active region. Inset: The flow-speed level of the active fluid was tuned by replacing processive motors (K401) with nonprocessive motors (K365) with the same overall motor concentrations (120 nM) (left)<sup>35,49</sup> or by altering the sample thickness (right).<sup>49,51</sup>

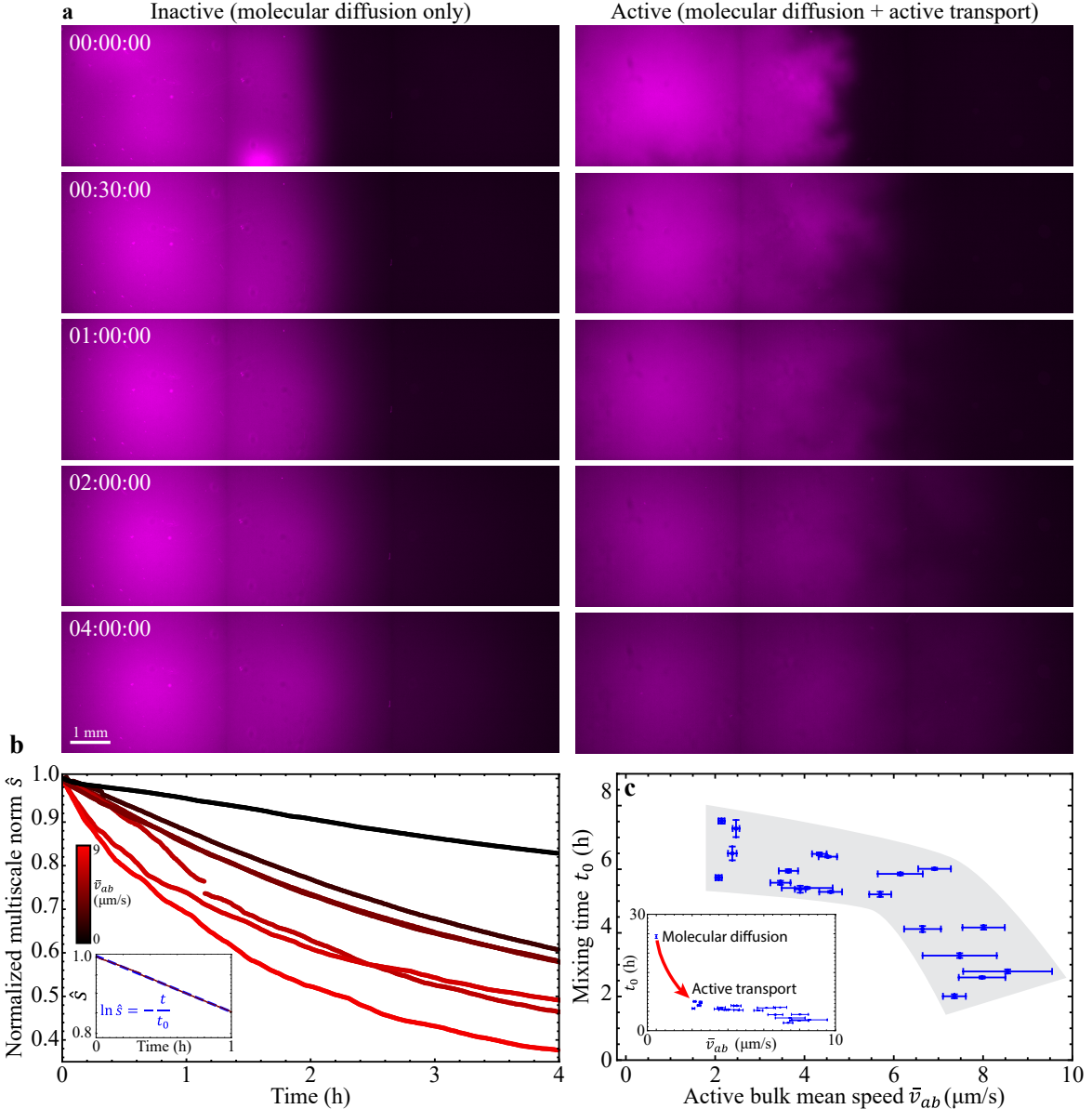


Fig. 5: Active fluid flows promoted mixing of UV-activated fluorescent dyes, which were initially activated in the left-hand side of the container only. (a) Dispersion of UV-activated fluorescent dyes in inactive ( $\bar{v}_{ab} = 0$ ; left column) and active ( $\bar{v}_{ab} = 8.2 \mu\text{m/s}$ ; right column) fluids. Active fluid flows actively transported fluorescent dyes (active transport) and enhanced their dispersion. Time stamps are hour:minute:second. (See also Supplementary Video 3.) (b) Selected examples of normalized multiscale norm versus time for different flow-speed levels,  $\bar{v}_{ab}$ . Normalized multiscale norm  $\hat{s}(t)$  decreased faster in a faster-flowing active fluid system. Inset: The normalized multiscale norm  $\hat{s}(t)$  in log-linear axes behaved as a straight line, suggesting that the norm decayed exponentially with time. The decay time scale  $t_0$  (or mixing time) was determined by fitting the normalized multiscale norm versus time data to  $\ln \hat{s} = -t/t_0$  with  $t_0$  as the fitting parameter (dashed blue line). (c) The mixing time decreased with the mean speed of fluids in the active region  $\bar{v}_{ab}$  (shaded gray area), indicating that accelerating active fluid decreased the mixing time and thus enhanced the system mixing efficacy. Each dot represents one experimental measurement. Error bars in  $t_0$  represent the slope fitting error in  $\ln \hat{s} = -t/t_0$  (Panel b inset) and error bars in  $\bar{v}_{ab}$  represent the standard deviation of flow speeds in the active region. Inset:  $t_0$  versus  $\bar{v}_{ab}$  with a wider scale in  $t_0$  to include the mixing time for inactive fluid ( $t_0 = 24 \text{ h}$  at  $\bar{v}_{ab} = 0$ ; top-left dot) where the dispersion of dyes was driven by their molecular diffusion. The mixing time was reduced to 8 hours as the fluid was minimally activated ( $\bar{v}_{ab} = 2 \mu\text{m/s}$ ) and the dispersion of dyes was governed by diffusion-like manner of active transport.

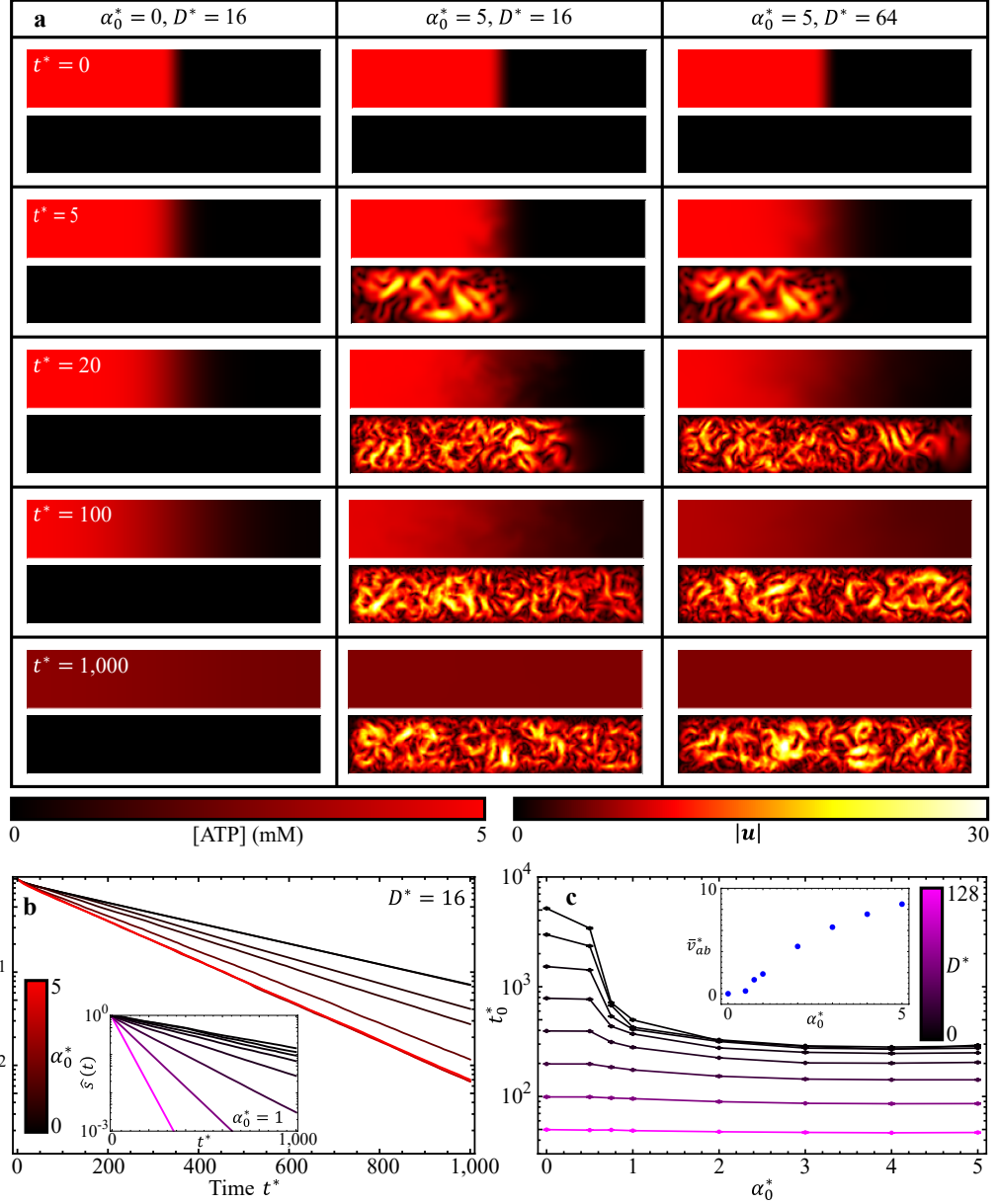


Fig. 6: A continuous active fluid simulation revealed that the mixing time of ATP depended on the dimensionless molecular diffusion coefficient of ATP and the dimensionless activity level of active fluid. (a) Table of ATP concentration (top) and active fluid flow speed (bottom) maps for various dimensionless activity levels  $\alpha_0^*$  and molecular diffusion coefficients  $D^*$ . When the fluid had no activity ( $\alpha_0^* = 0$ ; left column), ATP dispersed to the right side of the system only by molecular diffusion; the dispersion was enhanced when the active fluid started to flow and transport ATP ( $\alpha_0^* = 5$ ; middle column). The dispersion was further enhanced when ATP diffused significantly faster ( $D^* = 64$ ; right column) (Supplementary Video 4). (b) Evolution of normalized multiscale norm for  $\alpha_0^* = 0-5$  while keeping  $D^* = 16$ . The normalized multiscale norms decayed exponentially with time:  $\hat{s} = \exp(-t^*/t_0^*)$ , where  $t_0^*$  is the dimensionless mixing time. Inset: Evolution of normalized multiscale norm for  $D^* = 1-128$  while keeping  $\alpha_0^* = 1$ . The curves were colored based on the  $D^*$  color bar in Panel c. (c) The ATP dimensionless mixing times  $t_0^*$  as a function of dimensionless activity level  $\alpha_0^*$  for various dimensionless molecular diffusion coefficients ( $D^*$ ). The dimensionless mixing time decreased with increasing dimensionless activity level of active fluid until the molecular diffusion effect became so strong that the active transport mechanisms was negligible (purple and magenta curves). Each error bar in  $t_0^*$  represents the fitting error of  $\hat{s}$  versus  $t^*$  to  $\ln \hat{s} = -t^*/t_0^*$  (Panel b). Inset: Dimensionless mean speed of active fluid in active region  $\bar{v}_{ab}^*$  increases with dimensionless activity level  $\alpha_0^*$ .

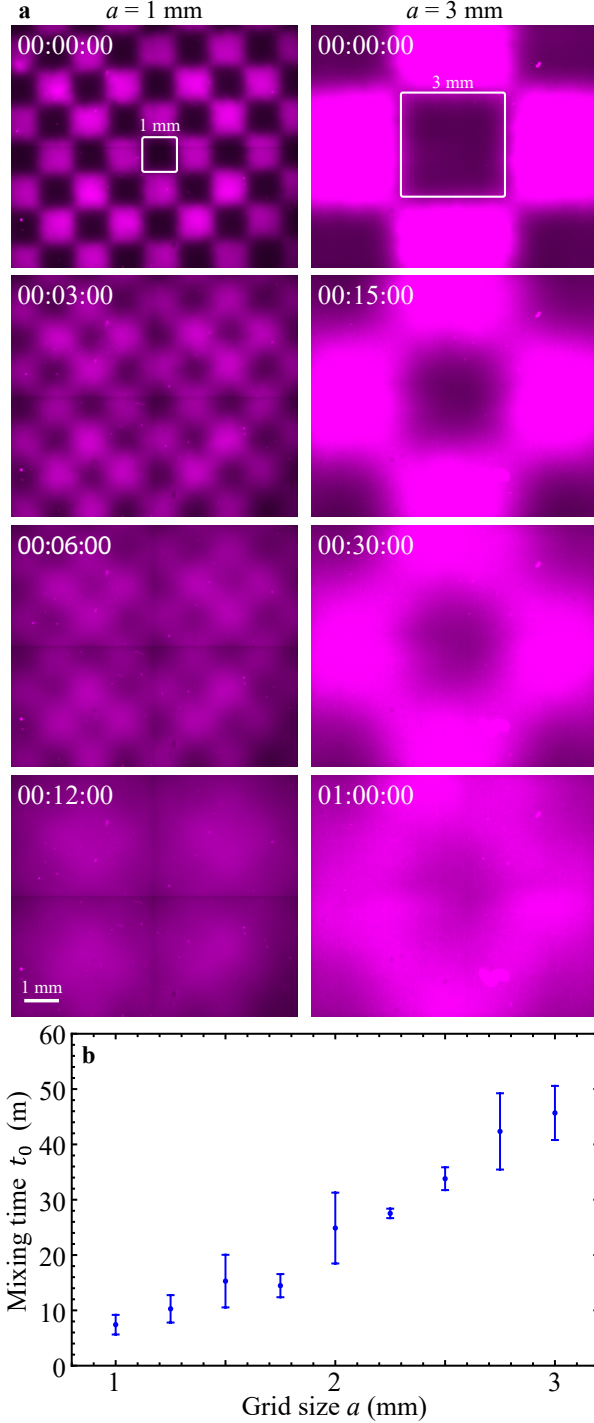


Fig. 7: Fluid activated in a checkerboard pattern mixed faster when the checkerboard grid was smaller. (a) Ultraviolet light activated active fluid with caged fluorescent dyes was activated with checkerboard-patterned UV lights. (Supplementary Video 5). (b) The mixing time of the checkerboard-activated fluid increased with grid size, which demonstrated that the mixing efficacy of active fluid depended on distribution of activity: the more nonuniform active fluid mixed the system more slowly. Each error bar in  $t_0$  represents the standard deviation of 2 trials.

**Supplementary Information:  
Self-mixing in microtubule-kinesin active fluid from nonuniform to  
uniform distributions of activities**

Teagan E Bate,<sup>1</sup> Megan E Varney,<sup>2</sup> Ezra H Taylor,<sup>1</sup> Joshua H Dickie,<sup>1</sup> Chih-Che Chueh,<sup>3</sup> Michael M Norton,<sup>4</sup> and Kun-Ta Wu<sup>1,5,6,\*</sup>

<sup>1</sup>Department of Physics, Worcester Polytechnic Institute, Worcester, Massachusetts 01609, USA

<sup>2</sup>Department of Physics, New York University, New York, New York 10003, USA

<sup>3</sup>Department of Aeronautics and Astronautics, National Cheng Kung University, Tainan 701, Taiwan

<sup>4</sup>School of Physics and Astronomy, Rochester Institute of Technology, Rochester, New York 14623, USA

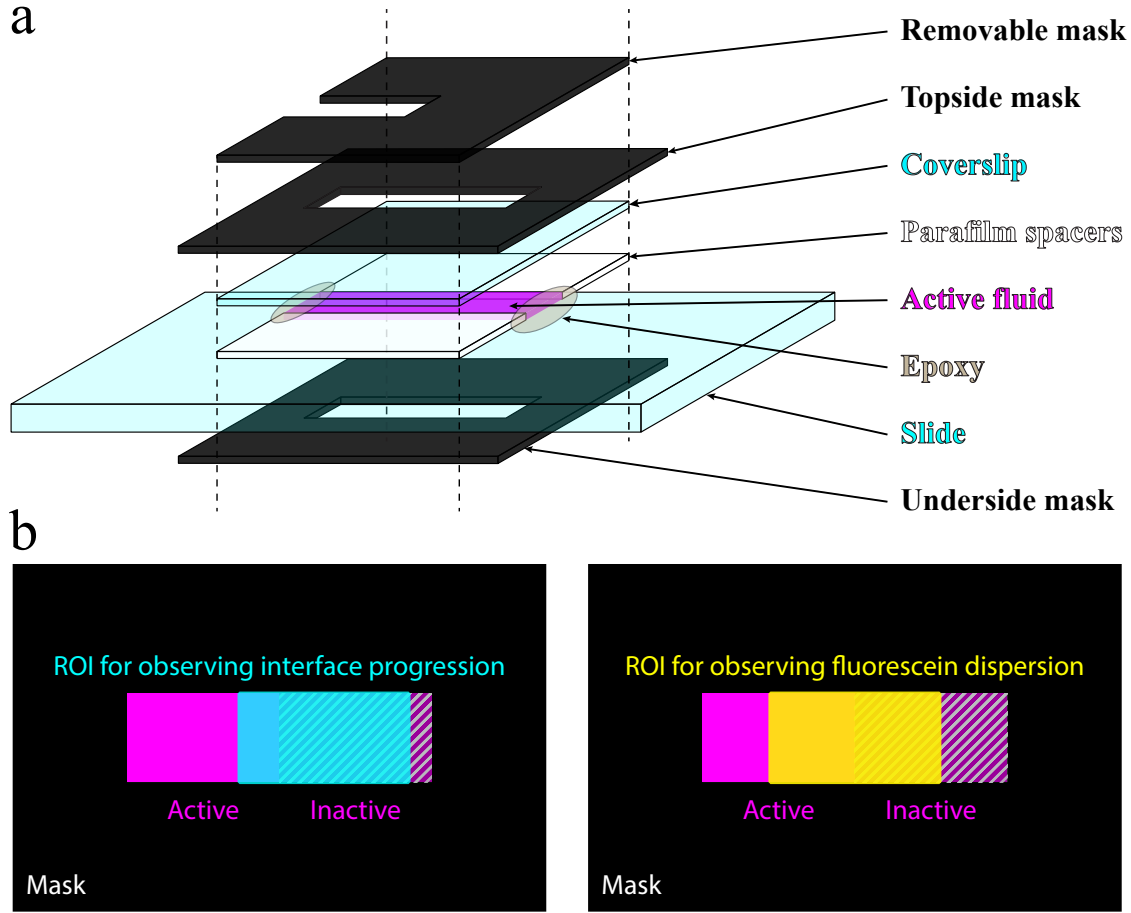
<sup>5</sup>Department of Mechanical Engineering, Worcester Polytechnic Institute, Worcester, Massachusetts 01609, USA

<sup>6</sup>The Martin Fisher School of Physics, Brandeis University, Waltham, Massachusetts 02454, USA

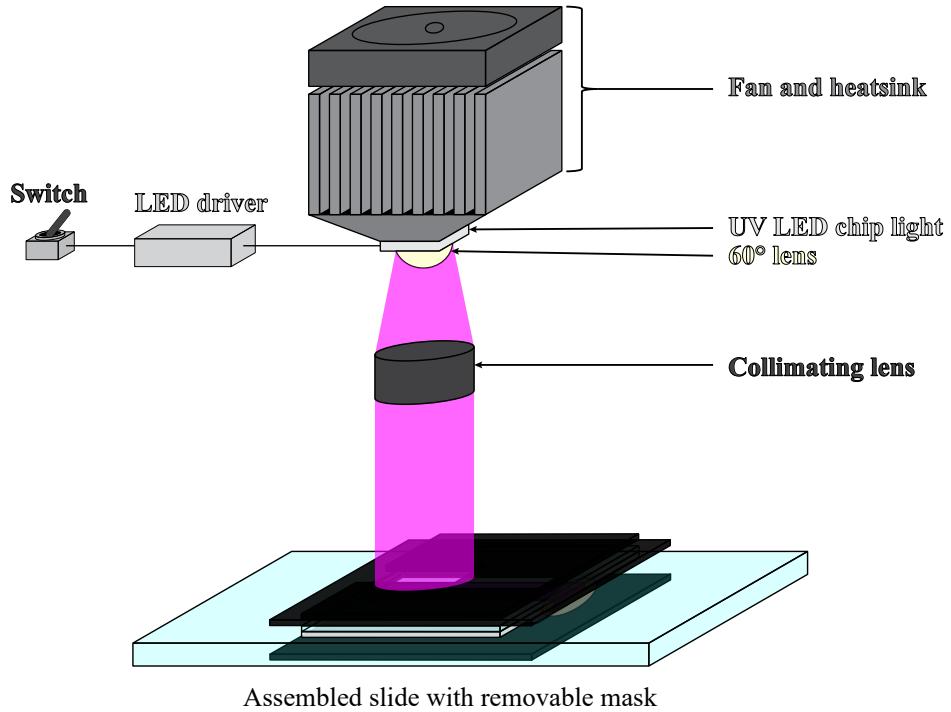
\*Corresponding: kwu@wpi.edu

**Table of Contents**

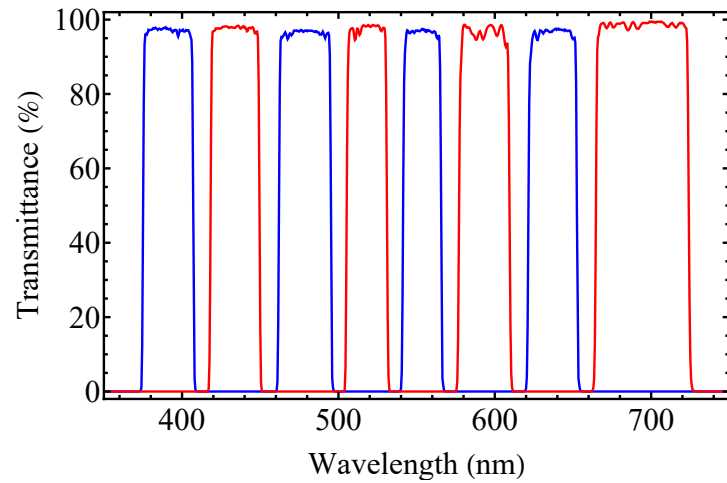
Supplementary Figures .....	2
Supplementary Videos .....	5
Supplementary References.....	6



Supplementary Fig. 1: We used a removable mask to activate one side of the sample. (a) Active fluid was loaded into a glass flow cell consisting of a polyacrylamide-coated glass slide and coverslip with parafilm as a spacer and sealed with epoxy. To prepare the active-inactive fluid system, we blocked one side of the sample (right half) with a removable mask. To prevent UV light from being scattered to the masked region by the epoxy and parafilm, which could cause unwanted fluid activation in the masked region, we further blocked the rest of the sample, including epoxy and parafilm, with 2 masks (one topside and one underside). After the UV exposure, we removed the mask to image the sample with fluorescent microscopy. (b) The sample is 20 mm long, which is wider than the field of view in our microscope even using a 4 $\times$  objective, so we imaged 3 to 4 adjacent frames along the flow cell and stitched these frames into one large image. For the experiments monitoring active-inactive fluid interface progression (left), we selected the region of interest (ROI) as one quarter of active area and most of the inactive area (cyan rectangle) to observe the progression of the interface (Figs. 1–4). For the experiments monitoring the dispersion of fluorescein (right), we selected the ROI as half of the active and half of the inactive regions (yellow rectangle) to observe how one-sided dyes dispersed to the rest of the sample (Fig. 5).



Supplementary Fig. 2: Setup to apply UV light to the masked sample (Supplementary Fig. 1a).<sup>1</sup> UV light was emitted with a UV LED chip (Amazon, B01DBZK2LM) powered by an LED driver (McMaster, 4305N124) and cooled with a fan-powered heatsink (Amazon, B01D1LD68C). To ensure that the light exposure was consistent across the sample, we parallelized the emitted UV light beams with a 60° lens (part of the heatsink) and a collimating lens (part of the microscope, Nikon, MEA54000).



Supplementary Fig. 3: Excitation (blue) and emission (red) spectra of our multiband pass filter cube (Multi LED set, Chroma, 89402-ET). The filter cube is compatible with the fluorescent spectra of fluorescein (excitation: 490 nm; emission: 525 nm), Alexa 488 (excitation: 499 nm; emission: 520 nm), Alexa 647 (excitation: 650 nm; emission: 671 nm), and Flash Red (excitation: 660 nm; emission: 690 nm). Data source: [www.chroma.com](http://www.chroma.com).

Supplementary Video 1: Mixing of activated and inactivated fluids. The fluid contained caged ATP, which could not fuel the kinesin motors until it was uncaged by exposure to ultraviolet light. After one side of the sample was exposed to ultraviolet light, the ATP molecules on that side of the sample were released and could fuel the kinesin motors to drive microtubules and create flows. The activated fluid blended with the inactive fluid until two fluids became one activity-uniform fluid. Cyan fibers are microtubules and red dots are tracers. The time stamp indicates hour:minute:second.

Supplementary Video 2: A one-dimensional, Fick's law-based model described how ATP distribution evolved from one side of a container to being uniformly distributed (top). The ATP was confined in a segment from  $x = 0$  to  $x = 20$  mm. The ATP distribution was converted to distribution of active fluid mean speed via Michaelis-Menten kinetics (Fig. 3b), which shows that initially only one side of the system was activated followed by evolution toward an activity-uniform state (bottom). Active fluid with a higher initial concentration of ATP (8 mM; red curve) evolved toward an activity-uniform state faster than active fluid with a lower initial concentration (1 mM; black curve). The time stamp indicates hour:minute:second.

Supplementary Video 3: UV-activated fluorescent dyes were suspended in inactive (top) and active (bottom) fluids. In the inactive fluid system, the dyes were dispersed only by molecular diffusion, whereas in the active fluid system, the dyes were further transported by active fluid flows and thus dispersed faster through the sample. Time stamp indicates hour:minute:second.

Supplementary Video 4: Simulated maps of ATP concentrations and flow speeds of active fluid for various pairs of  $\alpha_0^*$  and  $D^*$ . In the no activity system ( $\alpha_0^* = 0$ ; top), dispersion of ATP was driven only by molecular diffusion ( $D^* = 16$ ). When the fluid was activated ( $\alpha_0^* = 5$ ; middle), dispersion of ATP was mainly driven by active transport with the negligible contribution from molecular diffusion. However, when the ATP diffused significantly faster ( $D^* = 64$ , bottom), dispersion of ATP was driven mainly by ATP molecular diffusion with negligible contribution from active transport.

Supplementary Video 5: Checkerboard-patterned UV light (grid size  $a = 1$  mm) was applied to an inactivated fluid system (00:00:12–00:01:06), which released caged ATP to activate kinesin motors and power the active fluid (middle). The motion of microtubules stirred the surrounding solvent, which carried and mixed the fluorescent dyes (left) to a homogeneous state in 10 minutes (00:10:30). The right panel represents merged microscopic images of fluorescent dyes and microtubules. Time stamp indicates hour:minute:second.

## Supplementary References

- 1 Berezney, J., Goode, B. L., Fraden, S. & Dogic, Z. Extensile to contractile transition in active microtubule-actin composites generates layered asters with programmable lifetimes. *Proceedings of the National Academy of Sciences* **119**, e2115895119 (2022).